Naval Research Laboratory

Washington, DC 20375-5320

NRL/6790/MR--2021/1

Foundations for Autonomously Interacting Swarm Transformations: NISE Final Report

Ira B. Schwartz

Jason Hindes

Nonlinear Systems Dynamics Section
Plasma Physics Division

Victoria Edwards

Navy Center for Applied Research in Artificial Intelligence
Information Technology Division

January 7, 2021

REPORT DOCUMENTATION PAGE

Form Approved
OMB No. 0704-0188

1. REPORT DATE *(DD-MM-YYYY)*	**2. REPORT TYPE**	**3. DATES COVERED** *(From - To)*
07-01-2021	NRL Memorandum Report	June 2020 – September 2020

4. TITLE AND SUBTITLE

Foundations for Autonomously Interacting Swarm Transformations: NISE Final Report

5a. CONTRACT NUMBER

5b. GRANT NUMBER

5c. PROGRAM ELEMENT NUMBER
NISE

6. AUTHOR(S)

Ira B. Schwartz, Victoria Edwards, and Jason Hindes

5d. PROJECT NUMBER

5e. TASK NUMBER

5f. WORK UNIT NUMBER
1X33

7. PERFORMING ORGANIZATION NAME(S) AND ADDRESS(ES)

Naval Research Laboratory
4555 Overlook Avenue, SW
Washington, DC 20375-5320

8. PERFORMING ORGANIZATION REPORT NUMBER

NRL/6790/MR--2021/1

9. SPONSORING / MONITORING AGENCY NAME(S) AND ADDRESS(ES)

Naval Research Laboratory
4555 Overlook Avenue, SW
Washington, DC 20375-5320

10. SPONSOR / MONITOR'S ACRONYM(S)
NRL

11. SPONSOR / MONITOR'S REPORT NUMBER(S)

12. DISTRIBUTION / AVAILABILITY STATEMENT

DISTRIBUTION STATEMENT A: Approved for public release; distribution is unlimited.

13. SUPPLEMENTARY NOTES

14. ABSTRACT

In nature and robotics, autonomous swarms consist of mobile agents with limited dynamics and simple rules, which collaborate to produce emergent large-scale coherent behaviors. Such coherence is dynamic and arises in the form of stable and adaptive spatio-temporal patterns that self-organize. Examples of such robotic swarm dynamics for defense applications include autonomous radar jamming, targeting, tracking, and surveillance. Autonomous swarm behaviors depend on many factors ranging from communication strength to noise, latency, network topology, and the presence of opposing agents - all of which can be used to control and disrupt the intent of a swarm. A central and open problem in swarm theory involves examining the conditions in which swarms achieve stable self-organizing behavior, as well as how external and internal forces destabilize swarm dynamics. Such forces may come from changes in communication topology, attraction and repulsive forces, as well multiple interacting swarms, whereby one swarm can change the behavior of an-other.

15. SUBJECT TERMS

Swarms Dynamics Control Delay communication
Networks Bifurcations

16. SECURITY CLASSIFICATION OF:			**17. LIMITATION OF ABSTRACT**	**18. NUMBER OF PAGES**	**19a. NAME OF RESPONSIBLE PERSON**
a. REPORT	**b. ABSTRACT**	**c. THIS PAGE**			Dr. Ira B. Schwartz
Unclassified Unlimited	Unclassified Unlimited	Unclassified Unlimited	Unclassified Unlimited	57	**19b. TELEPHONE NUMBER** *(include area code)* (202) 404-8359

Standard Form 298 (Rev. 8-98)
Prescribed by ANSI Std. Z39.18

This page intentionally left blank.

Foundations for Autonomously Interacting Swarm Transformations: NISE Final Report[a)]

Ira B. Schwartz[1,*], Victoria Edwards[2], and Jason Hindes[1]

[1]*U.S. Naval Research Laboratory, Code 6792, Nonlinear Systems Dynamics Section, Washington, DC 20375, USA*

[2]*U.S. Naval Research Laboratory, Code 5514, Navy Center for Applied Research in Artificial Intelligence, Washington, DC 20375, USA*

[*]*ira.schwartz@nrl.navy.mil*

In nature and robotics, autonomous swarms consist of mobile agents with limited dynamics and simple rules, which collaborate to produce emergent large-scale coherent behaviors. Such coherence is dynamic and arises in the form of stable and adaptive spatio-temporal patterns that self-organize. Examples of such robotic swarm dynamics for defense applications include autonomous radar jamming, targeting, tracking, and surveillance. Autonomous swarm behaviors depend on many factors ranging from communication strength to noise, latency, network topology, and the presence of opposing agents - all of which can be used to control and disrupt the intent of a swarm. A central and open problem in swarm theory involves examining the conditions in which swarms achieve stable self-organizing behavior, as well as how external and internal forces destabilize swarm dynamics. Such forces may come from changes in communication topology, attraction and repulsive forces, as well multiple interacting swarms, whereby one swarm can change the behavior of another.

In this report we consider three main topics which address the open problems of emergent self-organizing swarms. First we consider how the stability of swarms change as functions of system parameters in the presence of range dependent communication networks by examining its bifurcation structure. Then we look at current mixed-reality experiments of swarm patterns to verify previous bifurcation analysis. Finally, we show how one swarm can change the behavior of another by colliding two swarms together.

Manuscript approved January 5, 2021.

[a)] DISTRIBUTION STATEMENT A. Approved for public release: distribution unlimited.

CONTENTS

I. TORUS BIFURCATIONS OF LARGE-SCALE SWARMS HAVING RANGE DEPENDENT COMMUNICATION DELAY

A. Background

Swarming behavior, which we define as the emergence of spatio-temporal group behaviors from simple local interactions between pairs of agents, is widespread and observed over a range of application domains. Examples can be found in biological systems over a range of length scales, from aggregates of bacterial cells and dynamics of skin cells in wound healing[1–3] to dynamic patterns of fish, birds, bats, and even humans[4–7]. These systems are particularly interesting because they allow simple individual agents to achieve complex tasks in ways that are scalable, extensible, and robust to failures of individual agents. In addition, these swarming behaviors are able to form and persist in spite of complicating factors such as delayed actuation, latent communication, localized number of neighbors each agent is able to interact with, heterogeneity in agent dynamics, and environmental noise. These factors have been the focus of previous theoretical research in describing the bifurcating spatial-temporal patterns in swarms, as seen for example in Refs.[8–11]. Likewise, the application of swarms have been experimentally realized in areas, such as mapping[12], leader-following[13,14], and density control[15]. To guarantee swarming behavior experimentally, control is typically employed[16–20] to prove convergence to a given state by relying on strict assumptions to guarantee the desired behavior. However, by relaxing certain assumptions, a number of studies show that even with simple interaction protocols, swarms of agents are able to converge to organized, coherent behaviors in a self-emergent manner; i.e. autonomously without control. Different mathematical approaches yielded a wide selection of both agent-based[4,5,7,21] and continuum models that predict swarming dynamics.[2,8,22]. In almost all models, since the agents have just a few simple rules, there exists only a relatively small number of controllable parameters. The parameter set usually consists of a self-propulsion force, a potential function governing attracting and repelling forces between agents, and a communicating radius governing the local neighborhood at which the agents can sense and interact with each other.

In both robotic and biological swarms, an additional parameter appears as a delay between the time information is perceived and the actuation (reaction) time of an agent. Such delays have now been measured in swarms of bats, birds, fish, and crowds of people[23–25]. The measured delays are longer than the typical relaxation times of the agents, and may be space and time

dependent. Robotic swarms experience communication delays which provide similar effects to the delay experienced in natural swarms. Incorporating stationary delays along with a minimal set of parameters in swarm models results in multi-stability of rotational patterns in space[26–30]. In particular, for delays that equal and fixed, one observes three basic swarming states or modes: Flocking, which is a translating center of mass, Ring state, where the agents are splayed out on a ring in in phase about a stationary center of mass, and a Rotating state, where the center of mass itself rotates.

Synthetic robotic swarms have communication delays that naturally occur over wireless networks, as a result of low bandwidth[31] resulting in delayed communication and multi-hop communication[32]. In cases where the delays are fixed and equal, and the communication occurs on a homogeneous network, it is known that delays create new rotational patterns , as has been verified both theoretically and experimentally[27,28]. However, in situations with robots, even simple communication models are based on the distance between agents[33,34]. Following from these models, if one assumes that the delays are range dependent, the problem becomes one of studying state dependent delays where delays depend implicitly on the relative positions between agents.

When placing swarms in realistic complex environments, delays are not necessarily a continuous function of range, but rather it is the increasing probability of delays increasing stochastically when agents move further away from one another beyond a certain radius[35,36]. That is, the rate of communication becomes spatially dependent, whereby near agents see a signal with a fast rate of communication, but due to shading and fading of signals, communication rates are slowed and complex outside a given radius. Underwater communication is an excellent swarm example where delays outside a significant radius impart rates of communication of one to two orders of magnitude greater than local communication rates[37].

The swarm model that follows takes a globally coupled swarm, and explicitly relaxes the fixed delay assumption, by including range dependent delay based on a fixed communication radius. We show that when range dependent delays are included, new frequencies are introduced and generate bifurcations to a torus. The result is a milling type of swarm that depends on just a few parameters. The results here are important for robotic swarming where one of the goals is to produce desired patterns autonomously, without external controls. The pattern formations predicted here show how delayed information, whether coming from communication, actuations, or both, impacts the stability of swarm states, such as ring and/or rotating states. By revealing those parameter regions where patterns are destabilized, we provide a comprehensive characterization of the autonomously

accessible swarm states in the presence of range-dependent delay.

B. The swarm model

Consider a swarm of delay-coupled agents in R^2. Each agent is indexed by $i \in \{1,\ldots,N\}$. We use a simple but general model for swarming motion. Each agent has a self-propulsion force that strives to maintain motion at a preferred speed and a coupling force that governs its interaction with other agents in the swarm. The interaction force is defined as the negative gradient of a pairwise interaction potential $U(\cdot,\cdot)$. All agents follow the same rules of motion; however, mechanical differences between agents may lead to heterogeneous dynamics; this effect is captured by assigning different acceleration factors (denoted κ_i) to the agents. In this paper, we assume $\kappa_i = 1$ for all i. For the effect of heterogeneity on the swarm bifurcations, see[9].

Agent-to-agent interactions occur along a graph $\mathscr{G} = \{\mathscr{V},\mathscr{E}\}$, where $\mathscr{V}$ is the set of vertexes v_i in the graph and $\mathscr{E}$ is the set of edges e_{ij}. The vertices correspond to individual swarm agents, and edges represent communication links; that is, agents i and j communicate with each other if and only if $e_{ij} \in \mathscr{E}$. All communications links are assumed to be bi-directional, and all communications occur with a time delay τ. That is, range dependence is not included. Let $r_i \in \mathbb{R}^2$ denote the position of the agent i and let $\mathscr{N}_i = \{v_j \in \mathscr{V} : e_{ij} \in \mathscr{E}\}$ denote its set of neighbors of agent i. The motion of agent i is governed by the following equation:

$$\ddot{\mathbf{r}}_i = \kappa_i(1-\|\dot{\mathbf{r}}_i\|^2)\dot{\mathbf{r}}_i - \kappa_i \sum_{j\in\mathscr{N}_i} \nabla_x U(\mathbf{r}_i(t),\mathbf{r}_j^\tau(t)), \tag{1}$$

where superscript τ is used to denote time delay, so that $\mathbf{r}_j^\tau(t) = \mathbf{r}_j(t-\tau)$, $\|\cdot\|$ denotes the Euclidean norm, and ∇_x denotes the gradient with respect to the first argument of U. The first term in Eq. 1 governs self-propulsion, where the speed has been normalized to unity. That is, without coupling the agents always asymptote to unit speed.

To analyze the dynamics of a large scale swarm, we use a harmonic interaction potential with short-range repulsion.

$$U(\mathbf{r}_i,\mathbf{r}_j^\tau) = c_r e^{-\frac{\|\mathbf{r}_i-\mathbf{r}_j\|}{l_r}} + \frac{a}{2N}\left\|\mathbf{r}_i-\mathbf{r}_j^\tau\right\|^2. \tag{2}$$

In Eq. 1, it is assumed that the communication delay, τ, is independent of the distance, or range, between any pair of agents. (Notice that the exponent of the repulsion term is independent of the

delay since the repulsion force is local.) With the addition of delays in the network, it was shown in homogeneous communication networks that in addition to the usual dynamical translating and milling (or ring) states, for sufficiently large τ, new rotational states emerge[27]. In particular, for a a given attractive coupling strength, there is a delay that destabilizes the periodic ring state into a rotating state, in which the agents coalesce to a small group and move around a fixed center of rotation; this behavior is quite different from the ring state where agents are spread out in a splay state phase. The rotating state is only observed with delay introduced in the communication network, and it appears through a Hopf bifurcation.

However, in real-world robotic swarms, communication delays are not uniform between all pairs of agents; delays may be stochastic or even state-dependent. For example, if agents are communicating over a multi-hop network, the delay will increase with the number of hops required to send a message from one agent to the other, and in general will scale with the separation between them. In order to handle range dependent delays, we will make an approximation that depends on a communication range radius.

1. Approximating range dependent delayed coupling

For the coupling term, we are interested in introducing an approximation to range based coupling delay. Since all communicating agents send signals with some delay, we compute relative distances defined as

$$D^{\tau}_{i,j} \equiv ||\mathbf{r}_i - \mathbf{r}^{\tau}_j||. \tag{3}$$

We define a Heaviside function, $H(x)$, that is zero when $x \leq 0$ and 1 otherwise, and we employ global coupling based on a spring potential. For our range dependent metric, we let $\varepsilon \geq 0$ denote the range radius. Suppose that when the separation between two agents is small, that is less than ε, then sensing between two agents is almost immediate. In practice, the time needed for sensing depends on several factors, such as actuation times, and so distances in practice are computed with delay. Therefore, we model the coupling term for the i^{th} agent as

$$\begin{aligned} C_i(\mathbf{r}_i, \mathbf{r}_j, \mathbf{r}^{\tau}_j, \varepsilon) = &-\frac{a}{N}(\nabla_x U(\mathbf{r}_i(t), \mathbf{r}^{\tau}_j(t)))H(D^{\tau}_{i,j} - \varepsilon) \\ &-\frac{a}{N}(\nabla_x U(\mathbf{r}_i(t), \mathbf{r}_j(t)))(1 - H(D^{\tau}_{i,j} - \varepsilon)), \end{aligned} \tag{4}$$

where the first coupling term has delay turned on since the distance is outside a ball of radius ε, while the second term has no delay since the distance is within the ε ball. The resulting swarm model with range dependence from Eq. 4 is now

$$\ddot{\mathbf{r}}_i = \kappa_i(1-\|\dot{\mathbf{r}}_i\|^2)\dot{\mathbf{r}}_i - \kappa_i \sum_{j\in\mathcal{N}_i} C_i(\mathbf{r}_i,\mathbf{r}_j,\mathbf{r}_j^\tau,\varepsilon). \tag{5}$$

If the delayed distance is within an ε ball, then we evaluate the coupling without delay. Otherwise the coupling is delayed. Thus the coupling function takes into account when delay is active or not between pairs of communicating agents, and depends on the range radius, ε.

The Heaviside function of the right hand side of Eq. 9 renders the differential delay equation derivatives discontinuous, and as such poses a numerical integration problem. To mollify the lack of smoothness, we approximate $H(x)$ by letting $H(x) \approx \frac{1}{\pi}\arctan(kx) + \frac{1}{2}$, where $k \gg 1$ and constant, and limits on the Heaviside function as $k \to \infty$.

Using only the delayed distance to compute a range dependent coupling assumes that any measurement is not instantaneous. If one were to be able to compute the ideal situation where delay would not be a sensing factor, then certain issues would need to be resolved, which we do not consider here.

2. Numerical simulations of full swarms

Examples of simulations using the swarm model with the range dependent coupling are shown below. Here the number of agents, $N = 150$, and the coupling strength, $a = 2.0$. For the remainder of the analysis, we set $c_r = 0$, and note that the attractors persist when the repulsive amplitude is sufficiently small[27].

Note that even when ε is very small, as shown in Fig. 1, we observe a mix of clustered states which are a combination of pure ring and rotation states. The agents tend to cluster into local groups, and the clusters move in clockwise and counter-clockwise directions as in the ring state. Here, however, the phase differences between agents are non-uniform. When examining a single random agent, as shown in Fig 2, it is periodic with a sharp frequency of rotation, and the relative positions of all individual agents are phase locked. When considering the center of mass of the

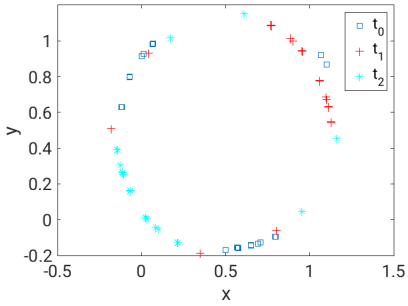

FIG. 1: Three snapshots of swarm state in space for $\varepsilon = 0.01, a = 2.0, \tau = 1.75$. Sample times $t_0, t_1 = t_0 + 20, t_2 = t_0 + 40$.

positions over all agents, $R \equiv \frac{1}{N}\sum_i r_i$, the center of mass does small amplitude oscillations about a fixed point (not shown).

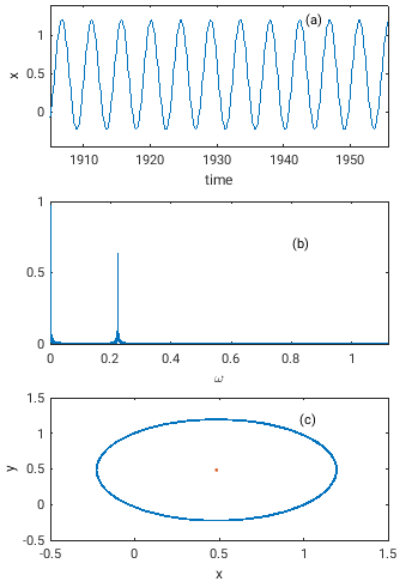

FIG. 2: Swarm ring state for $\varepsilon = 0.01, a = 2.0, \tau = 1.75$. (a)Time series of the x-component of a single agent. (b)The power spectrum showing a sharp frequency. (c)A phase portrait of the orbit of a single agent. The red point denotes the center of mass.

As the radius ε increases, instability of the periodic mixed state occurs, giving rise to more complicated behavior, as seen in Fig. 3. New frequencies are introduced, causing the ring state

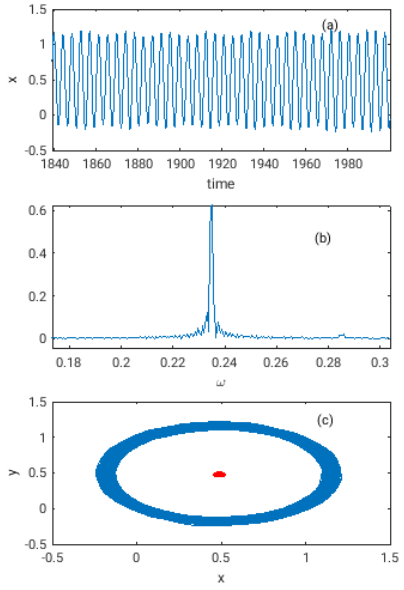

FIG. 3: Swam instability $\varepsilon = 0.25, a = 2.0, \tau = 1.75$. (a)Time series of the x-component of a single agent. (b)The Power spectrum showing a slight broadening and birth of a new frequency. (c)A phase portrait of the orbit of a single agent.

to appear as a quasi-periodic attractor. Moreover, the dynamics of the center of mass has its own non-trivial dynamics which includes the effects of new frequencies. By examining the Poincare map of the attractors, the instability gives rise to dynamics which we conjecture is motion on a torus. Letting (M_x, M_y) denote the time averaged center of mass over all agents, we compute the sequence $x(t_i), i = 1..M$ when $y(t_i) = 0$ and $x(t_i) > M_x$. The result is shown in the two panels in Fig. 4. Panel (a) shows a complicated toroidal motion after transients are removed of the center of mass in Fig. 3c. For a single frequency, the dynamics of the center of mass would be a single fixed point. The addition of new frequencies is revealed in the Poincare map as complicated motion on a torus. For larger values of ε, the motion on the torus converges to a periodic attractor in panel (b).

C. Mean-Field Equation of Range Dependent Delay Coupled Swarm

In order to shed some light on the origin of the bifurcation to dynamics on a torus, we examine the full swarm model from a mean-field perspective. The mean field is much lower dimensional, and a full bifurcation analysis may be done. We consider the case of all-to-all communication. Let

$$\boldsymbol{R} = \frac{1}{N}\sum_{i=1}^{N} \mathbf{r}_i$$

and

$$\mathbf{r}_i = \boldsymbol{R} + \delta\mathbf{r}_i,$$

where $\delta\mathbf{r}_i$ is a fluctuation term with the identity, and

$$\sum_{i=1}^{N} \delta\mathbf{r}_i = 0. \tag{6}$$

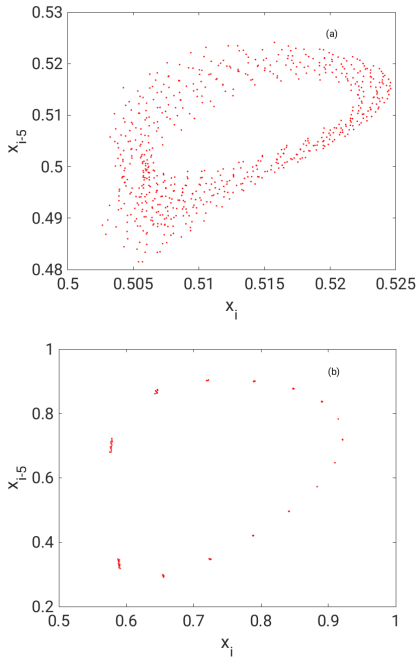

FIG. 4: Poincare map of Eqs. 1-4 for (a) $\varepsilon = 0.25$, (b) $\varepsilon = 0.5$. Other parameters are fixed: $a = 2.0, \tau = 1.75$. See text for details.

Then we can write Eq. 5 as

$$\begin{aligned}\ddot{\boldsymbol{R}}+\delta\ddot{\mathbf{r}}_i &= (1-|\dot{\boldsymbol{R}}+\delta\dot{\mathbf{r}}_i|^2)(\dot{\boldsymbol{R}}+\delta\dot{\mathbf{r}}_i)\\ &\quad -\frac{a}{N}\sum_{j=1,j\neq i}^{N}((\boldsymbol{R}+\delta\mathbf{r}_i)-(\boldsymbol{R}^{\tau}+\delta\mathbf{r}_j^{\tau}))C_{1,i}\\ &\quad -\frac{a}{N}\sum_{j=1,j\neq i}^{N}((\boldsymbol{R}+\delta\mathbf{r}_i)-(\boldsymbol{R}+\delta\mathbf{r}_j))C_{2,i}, \end{aligned} \tag{7}$$

where

$$\begin{aligned}C_{1,i} &= H(\|\mathbf{r}_i-\mathbf{r}_j^{\tau}\|-\varepsilon)\\ &= H(\|(\boldsymbol{R}+\delta\mathbf{r}_i)-(\boldsymbol{R}^{\tau}+\delta\mathbf{r}_j^{\tau})\|-\varepsilon)\\ &= H(\|\boldsymbol{R}-\boldsymbol{R}^{\tau}+\delta\mathbf{r}_i-\delta\mathbf{r}_j^{\tau}\|-\varepsilon)\end{aligned}$$

and

$$C_{2,i} = 1-C_{1,i}.$$

We use the following to reduce the equations of motion to the mean field: From Eq. 6, we note

$$\begin{aligned}\sum_{i=1}^{N}\delta\mathbf{r}_i^{\tau} = \sum_{j=1,j\neq i}^{N}\delta\mathbf{r}_j^{\tau}+\delta\mathbf{r}_i^{\tau} = 0 \iff\\ -\sum_{j=1,j\neq i}^{N}\delta\mathbf{r}_j^{\tau} = \delta\mathbf{r}_i^{\tau}.\end{aligned} \tag{8}$$

We further assume that all perturbations from the mean, $\delta\mathbf{r_i}$, are all negligible. (This is always true if the coupling amplitude is sufficiently large.) In addition, we use the fact that $\frac{a(N-1)}{N}$ limits to a, as $N\to\infty$. Therefore, we obtain mean field approximation for the center of mass of range dependent coupled delay case:

$$\ddot{\boldsymbol{R}} = (1-|\dot{\boldsymbol{R}}|^2)\cdot\dot{\boldsymbol{R}}-a(\boldsymbol{R}-\boldsymbol{R}^{\tau})\cdot H(\|\boldsymbol{R}-\boldsymbol{R}^{\tau}\|-\varepsilon) \tag{9}$$

D. Numerical Analysis of the mean field equation

1. Examples of rotational attractors

As in the case for the full multi-agent system, we see the existence of periodic behavior for τ sufficiently below an instability threshold, as shown in the time series of Fig. 5. As we increase τ, we expect the periodic orbit to lose stability, resulting in a new attractor. In particular, one notices

the emergence of a new frequency in addition to the existing dominant one, as shown in Fig. 6 The additional frequency usually implies a bifurcation to dynamics on a torus, or a higher dimensional torus.

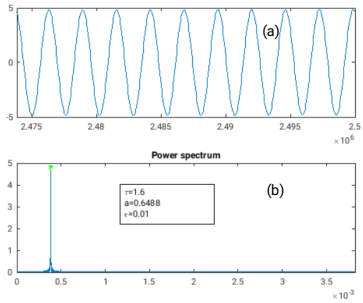

FIG. 5: Periodic motion of the mean field Eq. 9 for $\varepsilon = 0.01, a = 0.64, \tau = 1.6$. (a) Time series of the x-component of the mean field. (b) Power spectra of the time series.

We now investigate this transition by tracking the stability via monitoring the Floquet exponents corresponding to the periodic orbit. For a general differential delay equation given by $\dot{\boldsymbol{x}}(t) = \boldsymbol{F}(\boldsymbol{x}(t), \boldsymbol{x}(t-\tau))$, if $\boldsymbol{\phi}(t) = \boldsymbol{\phi}(t+T)$ for all $t \geq 0$, then stability is determined by examining the linearized equation along $\boldsymbol{\phi}(t)$:

$$\dot{\boldsymbol{X}}(t) = \frac{\partial \boldsymbol{F}}{\partial \boldsymbol{x}(t)}(\boldsymbol{\phi}(t), \boldsymbol{\phi}(t-\tau))\boldsymbol{X}(t) + \frac{\partial \boldsymbol{F}}{\partial \boldsymbol{x}(t-\tau)}(\boldsymbol{\phi}(t), \boldsymbol{\phi}(t-\tau))\boldsymbol{X}(t-\tau). \tag{10}$$

The stability of the periodic solution is determined by the spectrum of the time integration operator $U(T,0)$ which integrates Eq. 10 around $\phi(t)$ from time t = 0 to t = T. This operator is called the monodromy operator and its (infinite number of) eigenvalues, which are independent of the initial state, are called the Floquet multipliers[38]. For autonomous systems, it is necessary and sufficient there exists a trivial Floquet multiplier at 1, corresponding to a perturbation along the periodic solution[39,40]. The periodic solution is stable provided all multipliers (except the trivial one) have modulus smaller than 1; it is unstable if there exists a multiplier with modulus larger than 1. Bifurcations occur whenever Floquet multipliers move into or out of the unit circle. Generically three types of bifurcations occur in a one parameter continuation of periodic solutions: a turning point, a period doubling, and a torus bifurcation where a branch of quasi-periodic solutions originates and where a complex pair of multipliers crosses the unit circle[38].

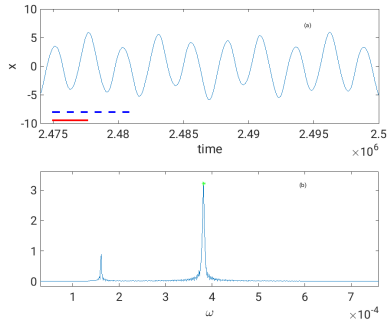

FIG. 6: Quasi-periodic motion of the mean field Eq. 9. (a) Time series of the x-component of the mean field. Solid (red) line denotes period length of dominant spectral peak. Dashed line denotes period length of secondary peak. (b) Power spectra of the time series.

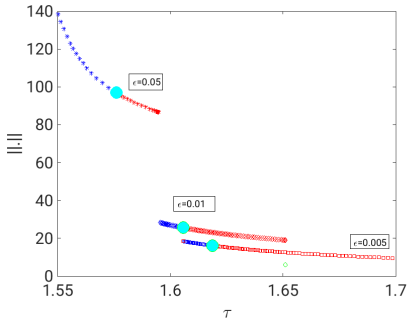

FIG. 7: Bifurcation plot showing the norm of the periodic orbits as a function of delay τ. Parameter a=0.68. Red (blue) markers denote unstable (stable) orbits.Cyan symbols denote the change in stability where a pair of complex eigenvalues cross the imaginary axis.

We have tracked a set of stable periodic orbits for various radii of ε, and located the change in stability by computing the Floquet multipliers. The results plotted in Fig. 7 show that for a range of radii ε, there exists a bifurcation to a torus at some delay. Notice that as ε increases, there results an increase in the size of the orbits, which qualitatively agrees with our full agent based simulations.

Since there exists a range of delays which destabilize periodic swarm dynamics for each ε, we summarize the onset of torus bifurcations by plotting the locus of points at which stability changes as a a function of coupling amplitude and delay. The results are plotted in Fig. 8.

Figure 8 is revealing in that it shows a functional relationship of the bifurcation onset that is similar over a range of ε. For larger values of ε, it is clear that lower values of delay and coupling are required to generate bifurcations. This holds true over two orders of ε. For a fixed value of ε, we also see monotonic relationship between delay and coupling strength, so that it is easier for smaller delays to destabilize periodic motion for larger coupling strengths.

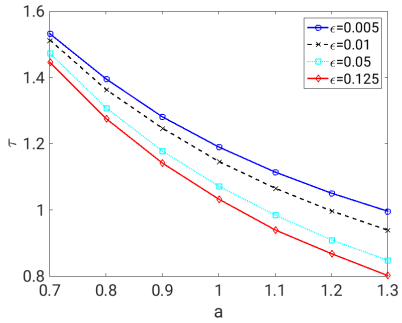

FIG. 8: Plotted is the locus of points at which torus bifurcations emerge as a function of coupling amplitude a, delay τ for various range radii ε for the mean field Eq. 9.

II. DELAY INDUCED SWARM PATTERN BIFURCATIONS IN MIXED REALITY EXPERIMENTS

A. Background

When examining biological swarms, recent analysis has shown that there exists a delay in reaction time between agents. In other words, as agents move, they react in response to the past positions of their neighbors rather than their instantaneously detected positions. For example, delays have been measured in schooling fish[50], bats[23], birds[24] and crowds of people[25]. Since natural agents move in an almost continuous manner, it is natural to model swarms based on biological ideas as continuous systems with communication delays.

Swarms can be modeled by differential delay equations where the delay is included in the communication network between agents. Such delays can act as a destabilizing parameter, which means for a swarm with communication delay different spatio-temporal patterns will emerge. Pattern emergence was shown by analyzing the mean field of a globally coupled swarm in the presence of communication delays where a Hopf bifurcation can be observed[26]. Recent work has generalized this result with an exact stability analysis and the inclusion of range dependent delay[51,52]. In Szwaykowska et al.[27], theoretical analysis showed that the delay-induced bifurcation picture is robust to random link removal in a swarm's communication network and to agent heterogeneity. Preliminary mixed reality experiments tested one of the theoretically predicted swarming behaviors for a restricted parameter set, but did not show transitions between swarm behaviors based on parameter changes.

In general, existing works in the design and control of artificial swarms have focused on the synthesis of local interaction rules that give rise to global swarm behavior. These works focus on bottom-up strategies where the objective is to develop provably correct single robot strategies that yield some desired swarm behavior[16–18,20,53–55]. Unsurprisingly, these works are based on a strict set of assumptions, which are necessary to ensure the desired emergent behavior. Nevertheless, while the strategies have been tested in simulation, validation on physical systems is often problematic since the necessary assumptions do not always hold in the real-world. Thus, the extensive body of work has provided a strong theoretical foundation for the design of swarming strategies but few have been experimentally validated on actual systems.

Experimental validation with physical robots invariably introduces uncertainty in the form of

actuation, sensing, and robot-robot and robot-environment interaction noise. Since swarms are complex nonlinear dynamical systems, they can typically exhibit multiple steady-state patterns[56]. In the presence of noise it is possible to transition from one steady-state to another[30,57]. Additionally, changes in system parameters can result in changes to the stability nature of steady-states[58–60]. In this work we conduct experiments with robots, which requires dealing with uncertainties inherent in physical experiments as well as changes in system parameters.

The dramatic reduction in the price to performance ratio of embedded processors, sensors, and computers and the ubiquity of wireless communications technologies have made experiments with ever larger number of robots more viable. Examples of these experiments include the Kilobots[61] which consists of 1000 robots interacting in a limited environment and the Crazyswarm[62] which consists of 50 unmanned aerial vehicles executing planned trajectories through the environment. Ultimately, the logistics of dealing with a large number of physical entities in a confined workspace require trade-offs: either the simplification of the environment or the use of open-loop, *e.g.*, precomputed, strategies that are not adaptive or reactive to changes in the environment or internal state of the swarm. Given these logistical challenges, experimental validation of swarming strategies are more often conducted using small numbers of robots which do not account for large number effects[15,63–66]. Unsurprisingly, experiments on small numbers of robots in controlled laboratory settings limit the types and frequency of robot-robot and robot-environment interactions. Furthermore, such methodologies cannot suitably evaluate the performance of the coordination strategies for arbitrarily large team sizes. Thus, the results may not fully account for the many factors that affect the dynamics of emergent swarming behavior.

In this work, we addressed these experimental challenges in engineered swarm systems by proposing a mixed reality experimental framework as a first significant step towards full experimental validation. Mixed reality is the use of both virtual robots and real robots in both the simulated and real world[67], that retains critical features of physical robots while enabling scaling to larger numbers of agents, or larger workspaces, without being subject to the physical limitations of resources. The benefits that come from mixed reality include: ability to work with large numbers of robots[68] and ensuring safety in human robot interactions[69–71]. Experiments using mixed reality come at a lower cost due to the reduced number of robots needed, while still introducing complex dynamics of the real world from a few real robots. Mixed reality is a significant first step towards full scale experimental validation of theoretical findings. Furthermore, the mixed reality framework provides opportunities to gain additional insights into the theory and improving

experiment design.

Our current research uses mixed reality as a way to further study the controller proposed in Szwaykowska et al.[27], and to map out experimentally a complete bifurcation picture in terms of physical parameters. In addition to uncovering the bifurcation structure of the swarm dynamics, we will focus on understanding transitions between behaviors and the impacts of adding collision avoidance. The new experiments are done using two different platforms of interest: one uses an Unmanned Aerial Vehicle (UAV), and the other uses an Autonomous Surface Vehicles (ASV), both within a mixed reality framework. The use of two different platforms has several advantages. First, it tests the universal bifurcation structure of delay coupled swarms across different platforms and vastly different time scales. Second, it allows for different numbers of robots and constraints to be tested safely during experimentation.

B. Methodology

Consider a swarm composed of N robots positioned in the plane, $r_i \in \mathbb{R}^2$, where $i \in 1...N$. We begin by detailing the development of our single agent and swarm ensemble models.

1. Single agent model

The dynamics for each agent in the system consist of a self propulsion term, an attraction term, and a repulsion term. This can be mathematically represented as follows using the original equation proposed by Mier-y-Teran-Romero[26] for the i^{th} agent:

$$\dot{r_i} = v_i, \tag{11}$$

and

$$\ddot{r_i} = (1 - ||\dot{r_i}||^2)\dot{r_i} - \sum_{j \in N} \nabla_{r_i} U[r_i(t), r_j^{\tau}(t)], \tag{12}$$

To model the communication topology between agents, we consider a fully connected graph model, $G = (\mathscr{E}, \mathscr{V})$, where $\mathscr{E}, \mathscr{V}$ are the set of edges and vertices, or nodes, respectively. We improve upon the validity of this model by having the robots communicate a delayed position

$r_j^\tau(t) = r_j(t-\tau)$. Note that the robots interact with one another with a fixed time delay, τ, which captures realistic finite-time effects of robot to robot communication.

We assume a harmonic interaction potential defines the attraction term

$$U(r_i, r_j^\tau) = f(r_i, r_j) + \frac{a}{2N}(r_i - r_j^\tau)^2, \tag{13}$$

where a is a constant, and $f(r_i, r_j)$ is a repulsion term.

In previous theoretical work the repulsion force was added to only a fraction of the agents in the experiments[27]. However, for real systems to interact safely in the world repulsion forces for all agent interactions are necessary, making it important to extend this work to consider the addition of repulsion to all agents in the swarm. As long as the repulsion force selected is an anti-symmetric function in the neighboring robot's states, the analysis performed in section II B 2 of the global swarm behavior will be preserved.

For the experimentation done in this paper, two anti-symmetric functions were selected. The original repulsion force presented in Szwaykowska et al.[27] is:

$$f(r_i, r_j) = c_r e^{\frac{||r_i - r_j||}{l_r}}, \tag{14}$$

where c_r is the strength of the repulsion, and l_r is the radius of repulsion considered between agents.

However, Equation 14 does not account for limitations of physical platforms, *e.g.*, max speeds or acceleration capacity. As such a sigmoid repulsion function is used:

$$f(r_i, r_j) = \left(c_r - \frac{c_r}{1 + e^{-k(|r_i - r_j| - R_{rep})}}\right)\frac{r_i - r_j}{|r_i - r_j|}. \tag{15}$$

where c_r is the maximum repulsion strength, R_{rep} is the inter agent distance at which the repulsion force is at half strength, and k represents how quickly the magnitude of the repulsion force switches from maximum strength to zero. Note that the repulsion term is independent of the delay since the interactions for repulsion are local in space.

2. Ensemble Swarm Model

The mean field of a swarm is computed by taking $R = \frac{1}{N}\sum_{i=1}^{N} r_i$ to denote the center of mass, and consider the limit as $N \to \infty$. From a mean field analysis of Equation 12, analytical expressions

can be derived for different swarm states[26]. The swarm state is the global representation of the entire swarm evaluated by observing the center of mass of the swarm, R, in lieu of the position of all agents. The state of the robot, r_i, is the individual dynamics for the local behavior of the robot.

The mean field of the original controller for the swarm behavior was shown theoretically to have several bifurcating regions in parameter space. Each region implies the stability of certain swarm behaviors including: flocking, ring, and rotating swarm states.

Figure 9(a) is the converted dimensional version of the original dimensionaless bifurcation structure proposed in Szwaykowska et al[27]. The transition between region II and III was theoretically predicted by a Hopf bifurcation curve of the mean field, and a pitchfork bifurcation curve is predicted to separate regions I and II. Figure 9(b) illustrates the three basic modal patterns of the swarm behavior as a function of the coupling strength, α, and communication delay, τ.

For the application of the dynamical model to the real world, we consider the dimensionalized equation for each agent as follows:

$$\ddot{r}_i = \beta(v_g^2 - ||\dot{r}_i||^2)\dot{r}_i - \frac{\alpha}{N}\sum_{j=1,j\neq i}^{N}(r_i - r_j^{\tau}) + \sum_{j=1,j\neq i}^{N}\nabla_r f(r_i, r_j), \tag{16}$$

where v_g m/s is the asymptotic velocity of the agent in the absence of coupling, α 1/s^2 is the coupling strength, β s/m^2 is a dimensional factor, and $\nabla_{r_i} f(r_i, r_j)$ is the repulsion force.

In order to further study the theoretically predicted swarm states, it was necessary to compute a new dimensional bifurcation diagram, which considers the physical parameters used in Equation 16. To achieve Figure 9(a) the following conversions were used:

$$t' = \beta v_g^2 t, \tag{17}$$

$$r_i' = \beta v_g r_i, \tag{18}$$

$$a = \frac{\alpha}{\beta^2 v_g^4}, \tag{19}$$

where a, t', and r_i' are dimensionless.

The conversion of the bifurcation diagram allows for regions of interest to be isolated, specifically around the regions of uncertainty along the Hopf bifurcation. The original mean-field analysis does not change through conversion, which is demonstrated in the appendix where the mean field was re-derived for Equation 16.

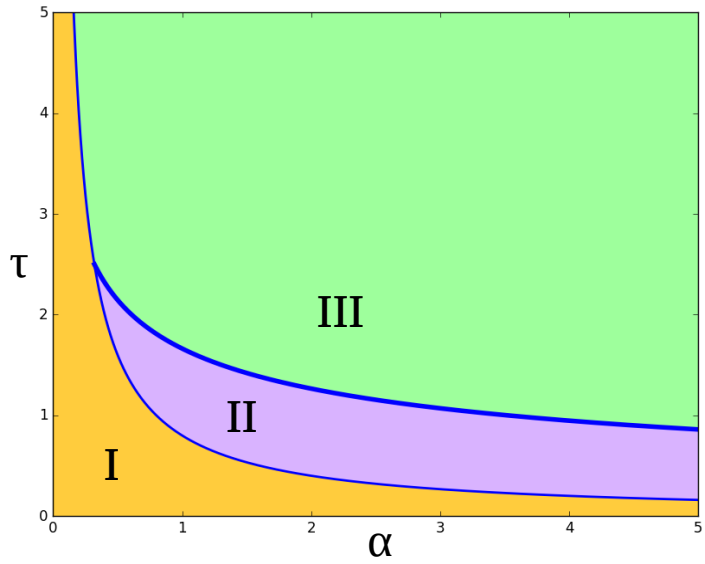

(a) Bifurcation Diagram

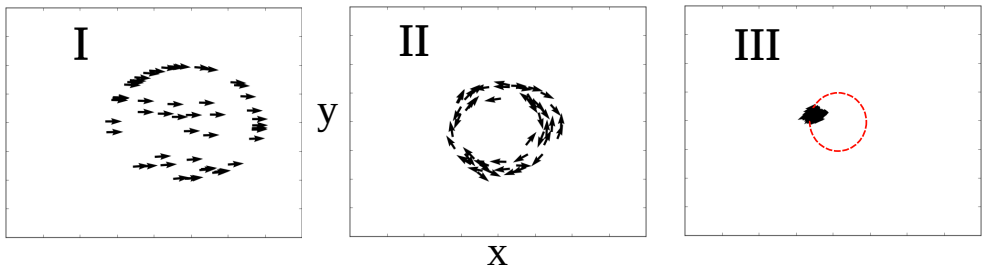

(b) Swarm States

FIG. 9: Figure 9(a): A bifurcation diagram as a function of communication delay, τ (s), and coupling amplitude, α (1/s^2) for the parameters used in UAV experiments: $\beta = 20.0$ s/m^2, $v_g = 0.2$ m/s. The solid curves are predicted from the mean field equations. The swarm is in a translating state with parameters from region I, and the swarm is in the rotating state with parameters from region III. In region II, the swarm is in a ring state, which also appears for parameters in region I and III. Note that for the ASV experiments different parameters were used, as such, a different bifurcation graph occurred meaning transitions between swarm states occurred for different parameter combinations. The ASV parameters were: $\beta = 18.0$ s/m^2 and $v_g = 0.047$ m/s. Additionally, repulsive forces impact the bifurcation structure and transition points, resulting in discrepancies from the mean-field predictions. Figure 9(b): The three possible swarm states are shown using 50 simulated agents (I Translating, II Ring, III Rotating).

The three desired swarm states are highlighted in Figure 9(a). In region I the swarm is in a translating state, where all agents are in alignment going in one direction. In region II the swarm is in a ring state, where all agents move about a stationary center of mass, and in region III the swarm is in a rotating state, where all agents cluster and move as a collective on a circular orbit around the origin. Along the boundaries of each region the swarm state will transition from one swarm state to another. This is referred to as the transition between swarm states. The possibility of multi-stable co-existing rotational patterns along these regions makes experimental verification important to further understand the limitations of the mean field analysis.

C. Experiments

The objective of our experiments is to test the mean field predictions described in Section II B in swarms composed of a few real robots. Discrepancies can then be used to build more accurate theories and analysis for future experiments with larger numbers of real robots. Mixed reality experiments were conducted using both the Ascending Technologies Inc. Pelican quadrotor shown in Figure 11(a) and custom built ASVs shown in Figure 11(b). We show experimentally all three swarm states (translating, ring, and rotating), along with the transition between swarm states as predicted by the bifurcation diagram in Figure 9(a) within the mixed-reality framework. We describe the details of our mixed reality architecture, experimental platforms, and experimental methodology in the following sections.

1. Mixed reality system architecture

An outline of a mixed reality system is in Figure 10(a), and an example of a mixed reality experiment is depicted in Figure 10(b). In building a mixed reality, global positions of the real robots are necessary, *e.g.*, GPS, infrared camera system, SLAM. The ground truth position of the robots are provided to the simulator, which maintains all simulated agents. The resulting response outputs for the robots are computed and sent to the robot from the simulator, considering interactions with all simulated agents.

The mixed reality system is controlled by the simulator, which maintains the positions of the simulated robots and updates the positions of the real robots based on ground truth information, as seen in Figure 10(a). The simulator workspace is defined as an unbounded region with no obsta-

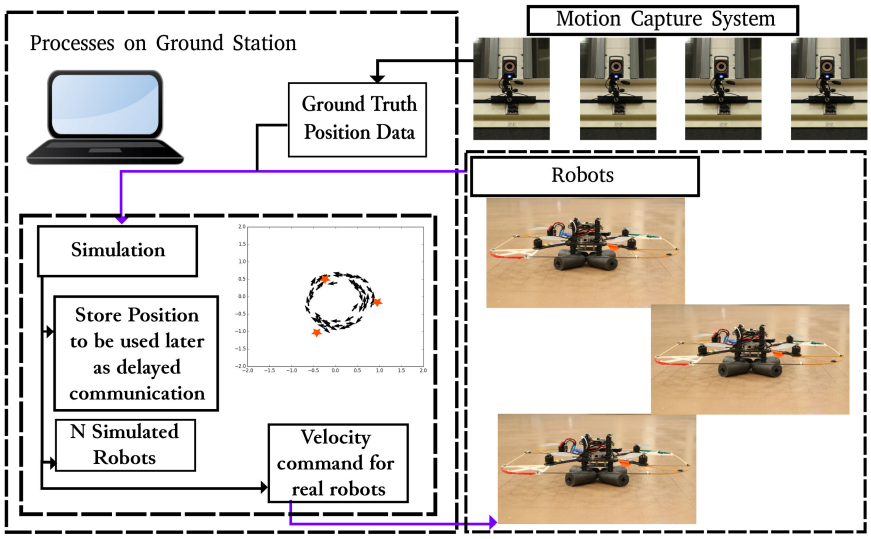

(a) Mixed reality Setup

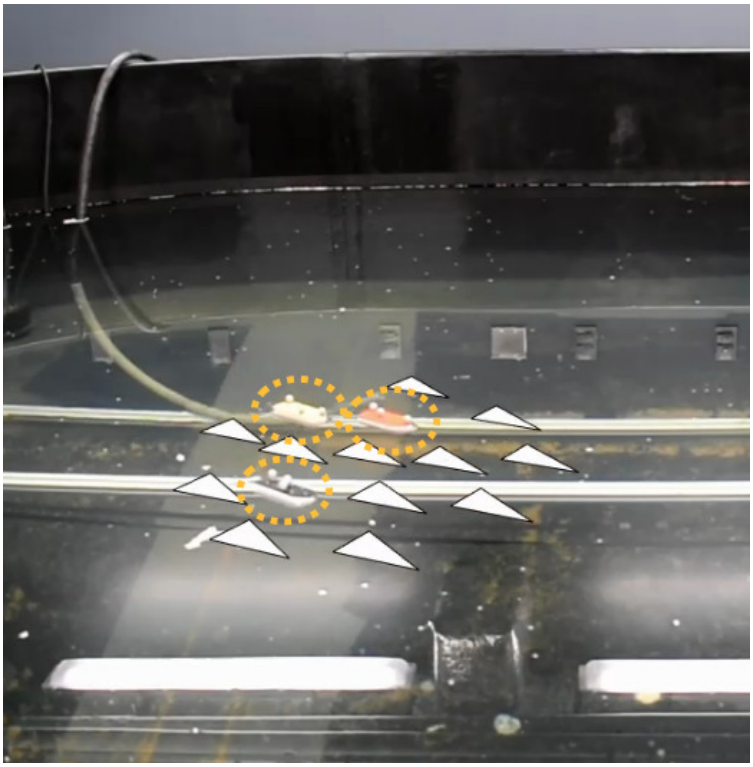

(b) Physical Example

FIG. 10: Figure 10(a): An outline for the mixed reality platform, where a ground station computer maintains the simulation and the state of the robot. The simulator is informed about the robot's state using a motion capture system to estimate of the robot's position, and the simulator sends new control outputs to the UAV. Figure 10(b): An example mixed reality setup for 3 ASVs and 12 simulated robots projected into image space.

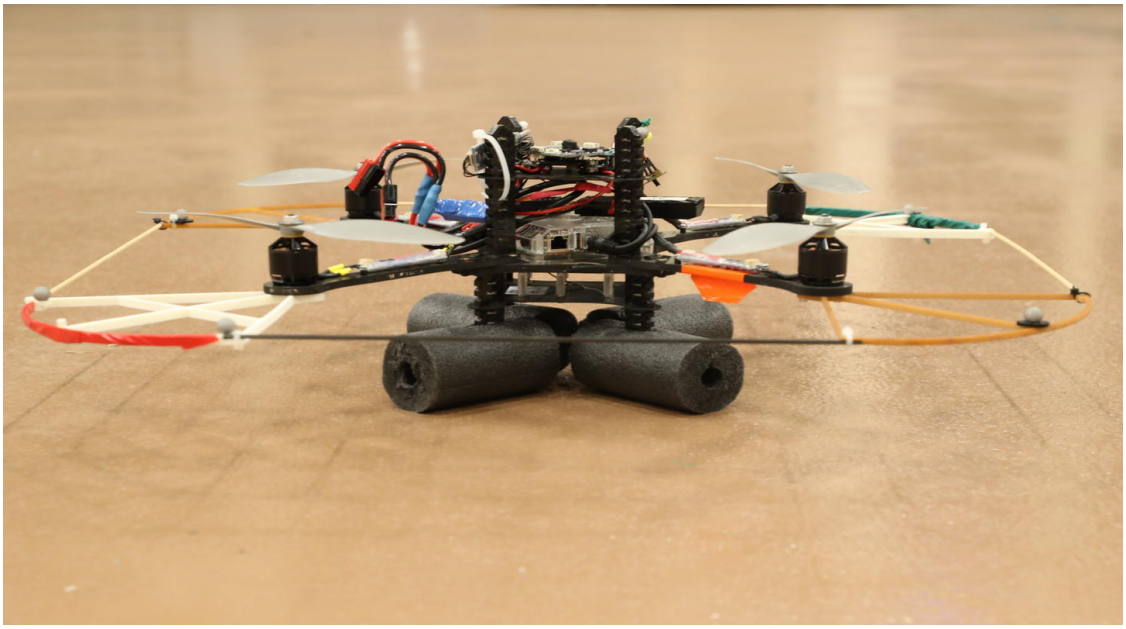

(a) Ascending Technologies Inc. Pelican Quadrotor

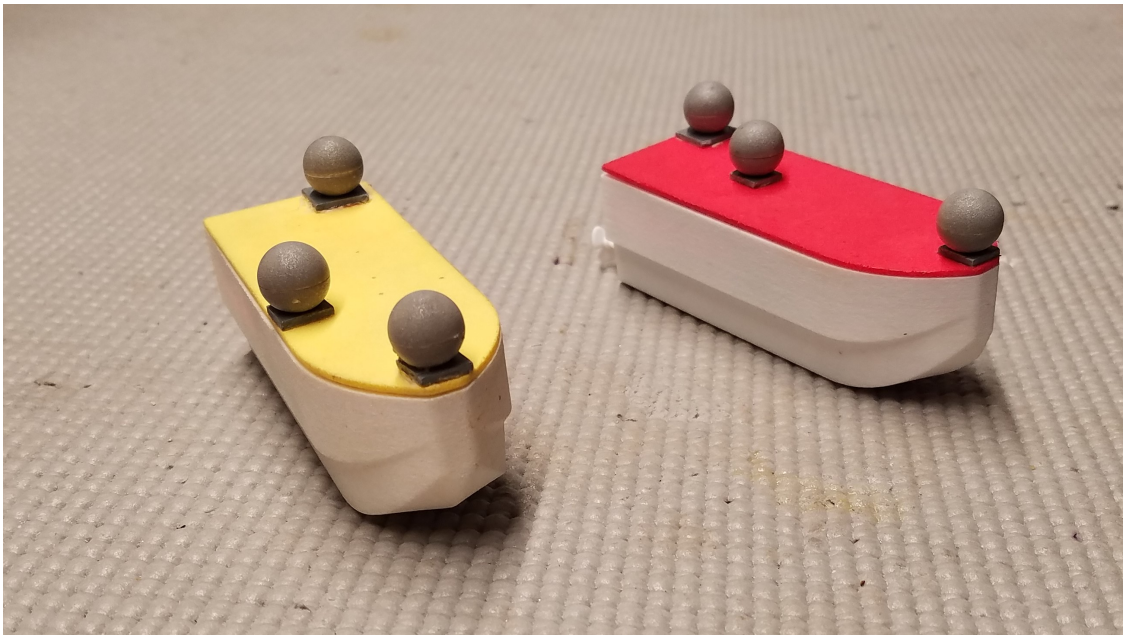

(b) Autonomous Surface Vehicle

FIG. 11: Figure 11(a) The Ascending Technologies Inc. Pelican Quadrotor, AscTec Pelican quadrotor. Figure 11(b) Autonomous Surface Vehicle, ASV, built at the University of Pennsylvania.

cles. The origin of the simulated workspace corresponds to the origin of the physical workspace. Delayed information is stored in a fixed length list for each agent which holds previous positions. The length of the list corresponds to the amount of delay specified: larger τ is a longer list, and smaller τ is a shorter list. The last entry in the list represents the delayed information received by an agent. All agents leveraged the global knowledge of the simulator to compute the distances between agents. Sensing between agents was abstracted away, which allowed for the focus of the results to be on the swarm states. From the simulator, new control commands were sent to the UAV/ASVs based on delayed information of simulated agents, as if they were in the world. Mixed reality allowed the UAV/ASVs to express the swarm behavior without the risk of multiple real robots interacting in unpredictable ways or the cost of running a multi-robot experiment.

2. Experimental Platforms

In this work we employed two experimental platforms: unmanned aerial vehicles (UAVs) and autonomous surface vehicles (ASVs). The validation using two separate platforms shows the applicability to any vehicle platforms whose dynamics can be abstracted into Equation 12. The UAV, Figure 11(a), is a quadrotor vehicle, which is equipped with an Odriod for onboard computing, WiFi communication, and an inertial guidance system (AscTec Autopilot). The vehicle is approximately 65.1 cm $\times$ 65.1 cm and 18 cm tall and weighs 1.65kg. The workspace is a 15m $\times$ 10m $\times$ 8m room. The ASVs, Figure 11(b), are differential drive surface vehicles equipped with a microcontroller board, XBee radio module, and an inertial measurement unit (IMU). The vehicles are approximately 12 cm long and have a mass of about 45g each. The ASVs are deployed in a 3 m $\times$ 5 m $\times$ 1m oval tank. Both workspaces include an infrared (IR) camera system to provide robot localization information.

3. Experimental Methodology

The experiments with the UAVs consisted of 1 physical and 49 simulated robots. The motions of simulated agents are updated using a double-point-integrator with Equation 16. For the translating swarm state, and the transition swarm state experiments the original configurations consisted of all agents facing in the same direction in a fixed pattern, with the same initial input velocity of 0.2 m/s. For the ring and rotating swarm state experiments, the UAV was placed at $[0,0,0]$ with

Swarm State	Duration	α 1/s^2	τ s	β s/m^2	v_g m/s	$\Delta\tau$
Translating	30	0.01	0.01	20.0	0.2	0.0
Ring	90	0.09	2.5	20.0	0.2	0.0
Rotating	90	1.0	4.0	20.0	0.2	0.0
Tran - Ring - Rot	200	1.5	0.01	20.0	0.2	0.3

TABLE I: Experimental parameters for UAV mixed reality experiments

the simulated robots placed around a rough ring shape with initial velocities in x and y selected between $[-0.3, 0.3]$ m/s. To achieve transition between swarm states $\Delta\tau$ was added every 10 s to τ. Details of experimental parameters are in Table I. Parameters were chosen for Equations (19) to satisfy maximum speed constraints for the real robots and finite workspace size. Using the theoretical equations predicting the ring and rotating state radii, parameters were selected which provided the desired radii size (≈ 0.75 m). The parameters were tested in simulation before being tested in experiments.

A small amount of repulsion was introduced to the experiment, Equation 14, where $c_r = 1.2$ and $l_r = 0.01$. To accommodate the low repulsion forces, the experiments were constrained to a two dimensional slice such that each real and simulated agent were on a unique plane. The interactions between agents were achieved by projecting all agents onto the same two dimensional plane, and velocities for the robot were a two dimensional velocity with an additional altitude component[72].

Next we considered the impacts of adding more robots to the swarm, thus requiring stronger repulsive forces. To do this we used a team of ASVs shown in Figure 11(b). The experiments consisted of 3 physical and 12 simulated robots. These experiments were specifically designed to observe transitions between swarm states by modifying the delay provided to the system. These were untested properties of the swarm model, and mixed reality allowed for testing theoretical predictions.

The parameters for the ASV mixed reality experiments are in Table II. For all experiments starting in the translating swarm state, the ASVs were initialized in a formation based on relative positions and moving forward at the desired speed v_g. For the experiment starting in the ring swarm state the ASVs were initialized at three equidistant points on a circle of radius 0.3 m pointing counter clockwise and tangent to the circle, and the virtual agents were initialized with random heading at points along the circumference of the circle with a normally distributed amount of

Swarm State	Duration	α 1/s^2	τ_0 s	β s/m^2	v_g m/s	τ_1 s
Tran-Ring-Rot	660	0.01	0.0	18.0	0.0471	10, 35
Tran-Rot-Tran	400	0.01	0.0	18.0	0.0471	35
Tran-Ring	300	0.01	0.0	18.0	0.0471	10
Ring-Rot	380	0.01	10.0	18.0	0.0471	35

TABLE II: Experimental parameters for ASV mixed reality experiments

noise added to their positions. Due to the physical constraints of the ASVs, sigmoid repulsion[73] (Equation 15) was used in Equation 16.

4. Experimental Evaluation

Evaluation of all experiments was done using swarm polarization, which is a measure of alignment between agents in a swarm. Swarm polarization is computed as follows:

$$sp = \frac{||\sum_i r_i||}{\sum_i ||r_i||}. \tag{20}$$

This metric evaluates the swarm state, for example; in the ring state all the individual positions of the agents will cancel out resulting in a swarm polarization of ≈ 0, while in the rotating and translating states the swarm is aligned resulting in a swarm polarization of ≈ 1. We note that swarm polarization has been proposed in earlier works,[74,75], and is a measure of alignment, but can be computed in different ways.

In addition to swarm polarization, the velocity of the center of mass and the acceleration of the center of mass were computed. These metrics aided in determining the difference between the translating and rotating swarm states, which have the same swarm polarization value. The rotating swarm state has a high velocity and acceleration of the center of mass, while in the translating swarm state the center of mass velocity is high but the acceleration is low. Velocity of the center of mass is computed as follows:

$$c_{vel} = ||\frac{\sum_i^N v_i}{N}||, \tag{21}$$

and the acceleration of the center of mass is:

$$c_{acc} = ||\frac{\sum_i^N \dot{v}_i}{N}||. \tag{22}$$

Additional comparisons were done using theoretically predicted results from equations in Szwaykowska et al.[27], and experimental results for the ring swarm state radius and period along with the rotating swarm state radius and period are presented in Figure 13. These equations are listed in the appendix.

D. Results

1. UAV Simulation of Parameters in Different Bifurcation Regions

Simulation trials using UAV parameters were executed with different combinations of α and τ, testing the theoretically predicted bifurcation regions in Figure 9(a). The simulation trials used parameters corresponding to the UAV experiments. The trials ran for 100 s, with $\beta = 20.0\,\text{s/m}^2$ and $v_g = 0.2\,\text{m/s}$. The initial $\alpha = 0.0\,1/\text{s}^2$ and $\tau = 0.01$ were the parameters used for the first trial. At the completion of a trial τ was updated by 0.5. The range of τ was $\tau \in [0.01, 5.51]\,\text{s}$ for each value of alpha. When a trial for each value in the range of τ was complete α was updated by 0.25. The range of α was $\alpha \in [0.0, 4.75]\,1/\text{s}^2$. In total, two hundred and forty simulation trials were run with 50 simulated agents. Figure 12 shows the resulting plot of the final swarm polarization at the end of each simulation, for each set of parameters, which shows fair qualitative agreement with mean field predictions.

Regions of multi-stability exist along the transition between swarm states, meaning that for certain initial conditions the swarm will transition to another swarm state or it may stay in the same swarm state[56]. This is clearly seen by the jagged edge along the bifurcation in Figure 12. This result showed that more experimentation using physical robots needed to be done, exploring each of the three swarm states along with transitions between the swarm patterns.

2. UAV Mixed Reality Results

The first set of experimental results used a UAV mixed reality framework. Experiments of the swarm in the translating swarm state were achieved using parameters from region I in Figure 9(a), where all agents move with the same average velocity. The swarm would quickly start moving out of the translating swarm state and into the ring swarm state in the last seconds of the experiment. This was due to the instability of the swarm when translating, from the introduction of any noise in the system, which can switch the system out of the translating swarm state and into the ring

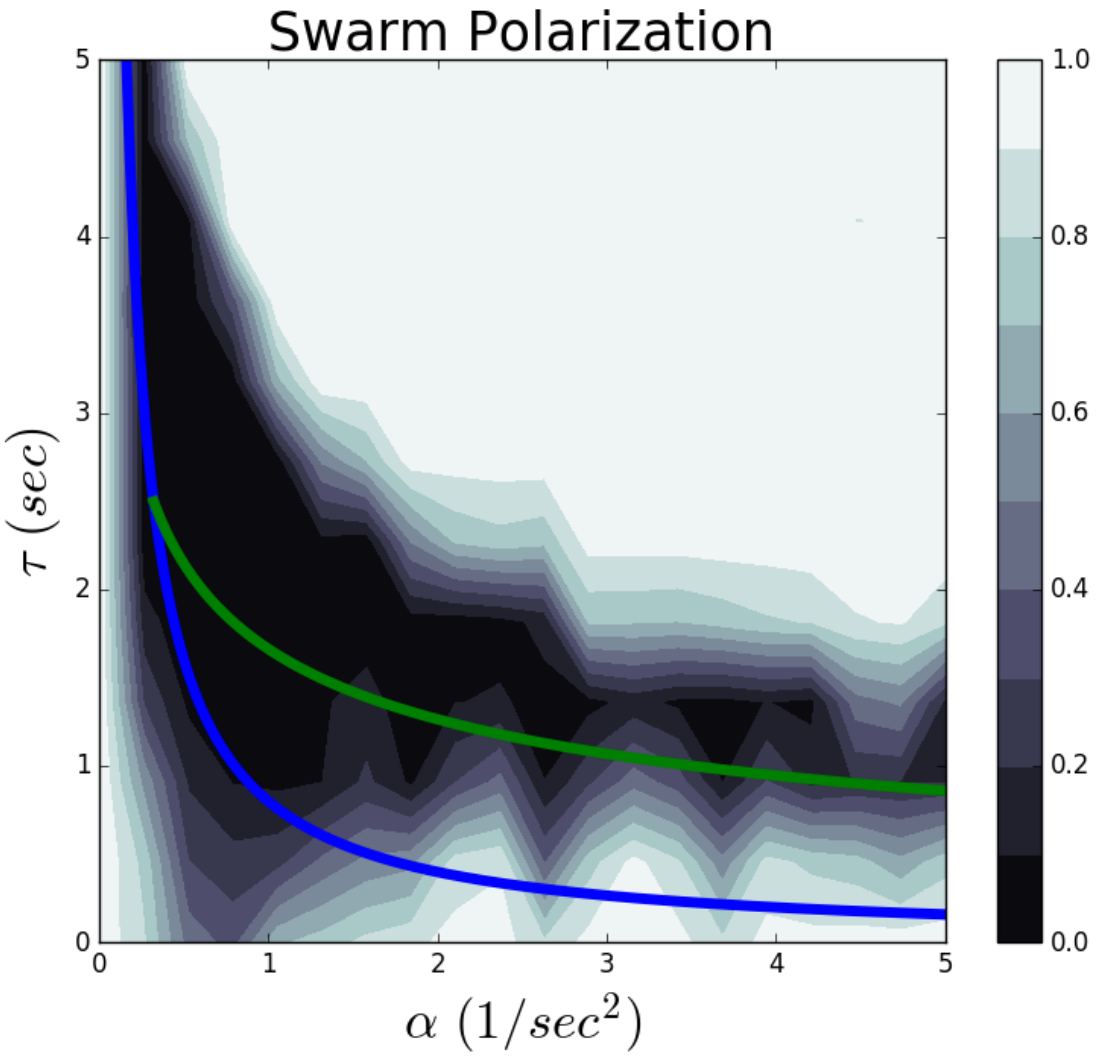

FIG. 12: The resulting swarm polarization from 240 simulation trials with 50 simulated agents. Each trial was 100 s and used UAV parameters, $\alpha \in [0.0, 4.75]$ 1/s^2, $\tau \in [0.01, 5.51]$ s, $\beta = 20.0$ s/m^2, and $v_g = 0.2$ m/s. For each α, τ was updated by 0.5 s. At the end of the range for τ, α was updated by 0.25 1/s^2. Color is a representation of the final swarm polarization at the end of an experiment. The trends of the contours while slightly off of the theoretically predicted bifurcation curve still meet the general trend of the plot. A transition from white to black to white in the plot, corresponds to the transition from the translating to ring to rotating swarm states.

swarm state.

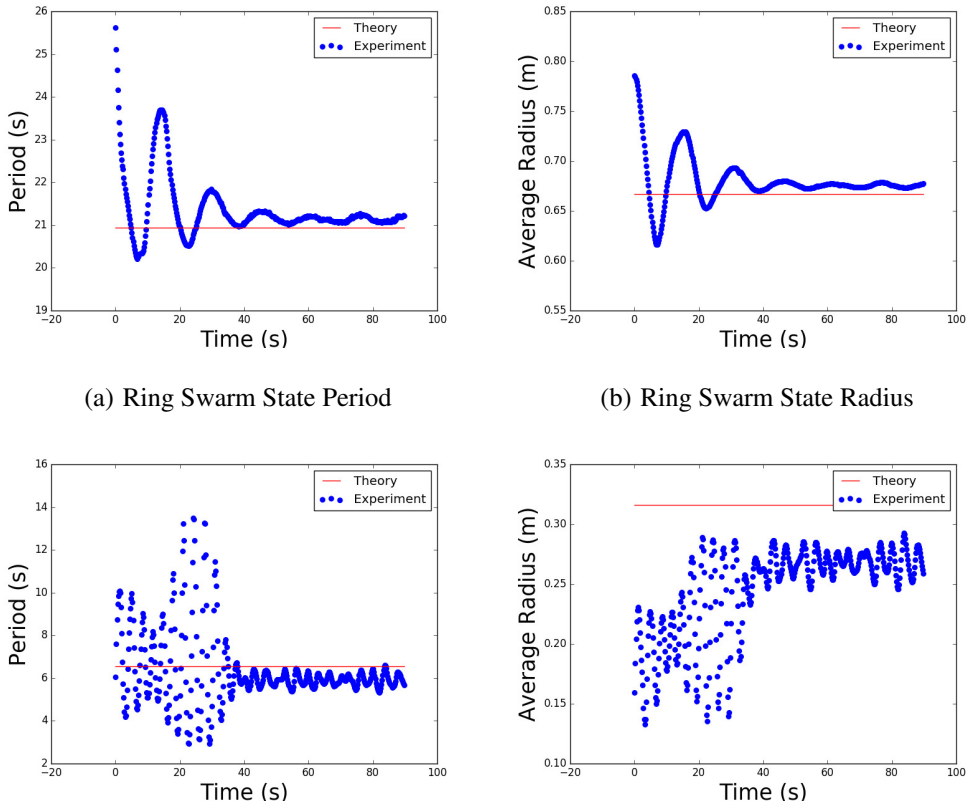

(a) Ring Swarm State Period

(b) Ring Swarm State Radius

(c) Rotating Swarm State Period

(d) Rotating Swarm State Radius

FIG. 13: Figure 13(a) and 13(b): Results from a 90.0 s ring experiment, which compared the theoretically predicted radius and period (red line), to the average for the swarm of the exhibited radius and period during a ring experiment (blue points). Figure 13(c) and 13(d): Results from a 90 s rotating experiment, which compared the theoretically predicted radius and period (red line), to the average for the swarm of the exhibited radius and period during a rotating experiment (blue points).

Experiments where the ring swarm state was expressed used parameters from region II in Figure 9(a), where all agents move, clockwise or counter-clockwise, around a stationary center of mass. To further test that the dynamic model matched experimental results, comparisons were made between the theoretically predicted radius and the period of the ring swarm state to the experimental values. Figures 13(a) and 13(b) show the average swarm ring period and radius experimental result (blue points) and the theoretically predicted value (red line). These experiments show that at steady-state the average swarm ring radius converges to approximately 0.68 m and

the average swarm ring period converged to approximately 21.22 s, these values were both close to the theoretically predicted values of 0.66 m and 20.94 s. To achieve the experimental ring radius and ring period, parameters were selected which put the swarm clearly in the ring swarm state. The theoretical values were computed based on the parameters selected for the experiments. The proximity of the measured ring radius and ring period comes from ensuring well calibrated experiments which expressed the desired behavior. This result qualitatively supports the comparison between the swarm theory and the experimental results.

The rotating swarm state experiments used parameters from Region III in Figure 9(a). During the rotating swarm state experiment all agents clustered together and moved in a collective around a stationary point. Figures 13(c) and 13(d) show the average radius and period of the swarm in the rotating state, comparing the theoretically predicted values (red line) to the experimental results (blue points). The theoretical period was 6.55 s and the theoretical radius was 0.32 m, compared with the converged average of the experimental period was 5.68 s and the experimental radius was 0.26 m. Similarly to the experiments with the swarm in the ring state, parameters were specifically selected to put the swarm clearly in the rotating swarm state. The measured rotating radius and rotating period are close to theoretical predictions because of well tuned experiments resulting in the desired behavior. The plots highlight that the swarm does converge to the theoretically predicted swarm behavior even with the addition of a real robot.

Finally, Figure 14 depicts the experimental results from an experiment transitioning through all three swarm states. The translating swarm state had swarm polarization of ≈ 1, a low center of mass acceleration, and a high center of mass speed. The speed of the center of mass decreased rapidly, with the addition of greater values of τ causing the swarm to begin to switch into the ring swarm state. The transition to the ring swarm state occurred between $\tau = [1.8, 2.41]$ s, where the swarm had a stationary center of mass resulting in 0 swarm polarization, 0m/s center of mass speed, and 0 m/s^2 center of mass acceleration. The final transition to the rotating swarm state occurred between $\tau = [3.61, 4.21]$ s, resulting in a swarm polarization of ≈ 1, a high center of mass acceleration, and a high center of mass speed. Although qualitatively accurate, the existence of small discrepancies between predicted and measured dynamics for a swarm with a single real UAV suggests the need for a more accurate description of the UAV dynamics.

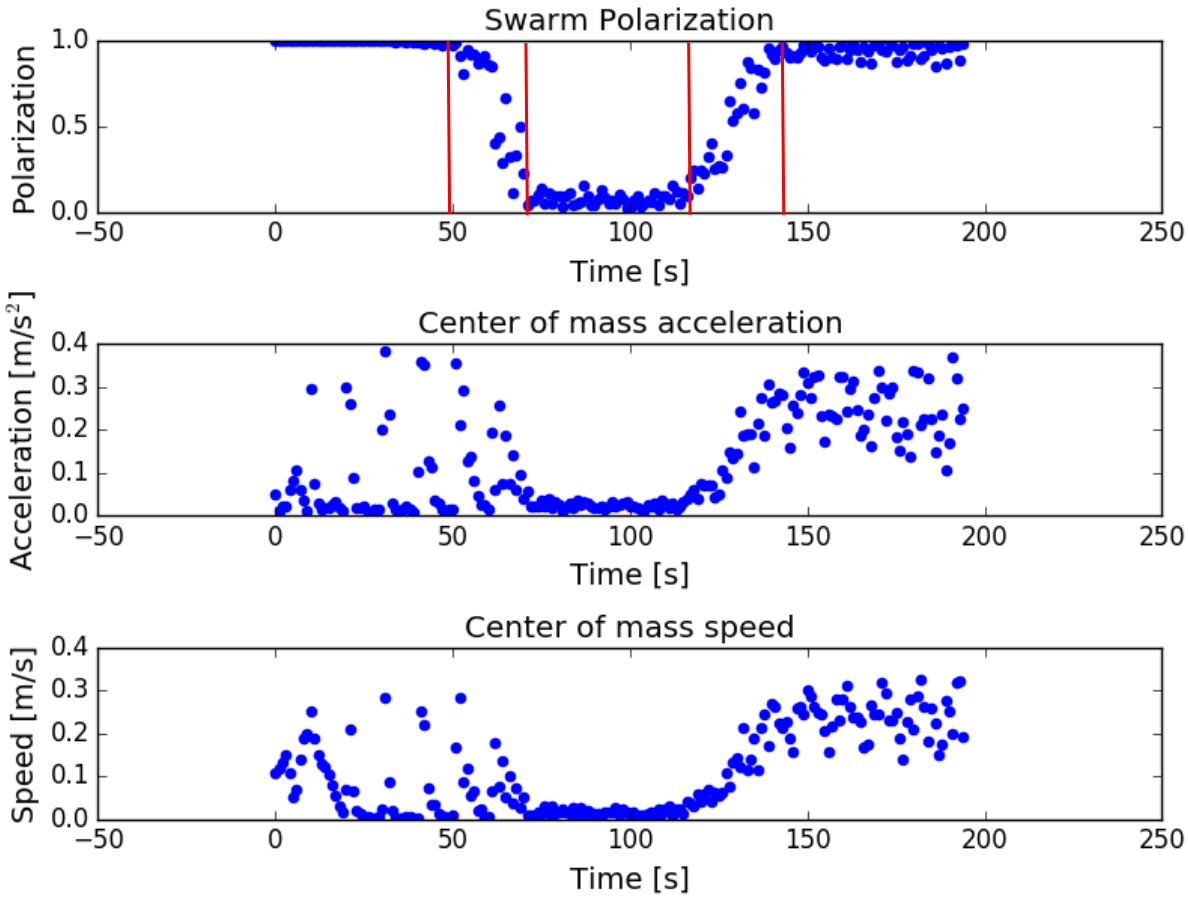

FIG. 14: Swarm polarization, center of mass acceleration, center of mass speed for an experiment with 1 UAV and 49 simulated robots. A 200 s experiment transitioning between translating, ring, and rotating swarm state, where the experiment started with the following parameters $\alpha = 1.5\,1/s^2$, $\tau_0 = 0.01$ s, $\beta = 20.0\,s/m^2$, $v_g = 0.2$ m/s, and every 10 seconds τ was updated by $\Delta\tau = 0.3$ s. The increment in tau caused the transition between the translating state to the ring state to occur between $\tau = [1.81, 2.41]$ s and the transition from the ring to the rotating state to occur at $\tau = [3.61, 4.21]$ s, labeled on the plot by red lines.

3. ASV Mixed Reality Results

ASV mixed reality experiments were performed to further investigate the transition between swarm states, and safely increase the number of robots. These experiments consisted of 3 ASVs and 12 simulated robots. Each experiment had multiple trials of different types of sigmoid repulsion[73]. The first ASV mixed reality experiments tested the transitions between all three swarm states. Additional experiments tested the transitions from translating swarm state to rotat-

ing swarm state, from the translating swarm state to the ring swarm state, and finally from the ring swarm state to the rotating swarm state.

The results from the experiments are presented in the following figures. Figure 16 depicts results from the translating to rotating swarm transition. The behavior of the swarm during the translating to ring swarm state transition is observed in Figure 15. Finally, results for the transition between the ring to rotating swarm state are presented in Figure 17.

From the experimental results we observed and measured the different theoretically predicted swarm states. The ring swarm state can be identified by the low swarm polarization, center of mass acceleration, and center of mass speed indicative of an unaligned swarm that is stationary. The rotating swarm state can be identified by the high polarization, center of mass acceleration, and center of mass speed indicative of an aligned swarm that is constantly moving in a circle. All of these traits can be seen in Figure 17. The oscillations in the center of mass speed and acceleration, in Figure 17, were the result of the swarm moving on an ellipsoidal trajectory, slowing down near the loci and speeding up near the semi-minor axis. The dips in the polarization were the result of the existence of two groups of agents in the swarm that turn in different directions when the whole swarm reverses direction near the loci of the ellipse. The ellipsoidal motion gradually relaxed to a circle with all of the agents turning together in the same direction, with center of mass acceleration and velocity reaching steady state values and the polarization approaching a steady state value of 1.

Likewise, in Figure 15 there is a spike in polarization around the 50s mark. This was due to the swarm reversing direction coherently before scattering into the ring swarm state. In the translating and rotating swarm state, the ASVs adopted a hexagonal grid formation in the rough shape of a disk that remained rigid even during transitions between the rotating and translating state.

The experimental results successfully reproduced and extended the results obtained from the mixed reality UAV experiments described in section II D 2. The ASV mixed reality experiments showed the persistence of the swarm states and the transition between the states even when collision avoidance routines were executed on all robots and virtual agents. These results are a step towards experimental validation because full scale robot experiments will require collision avoidance for safe robot-robot interactions.

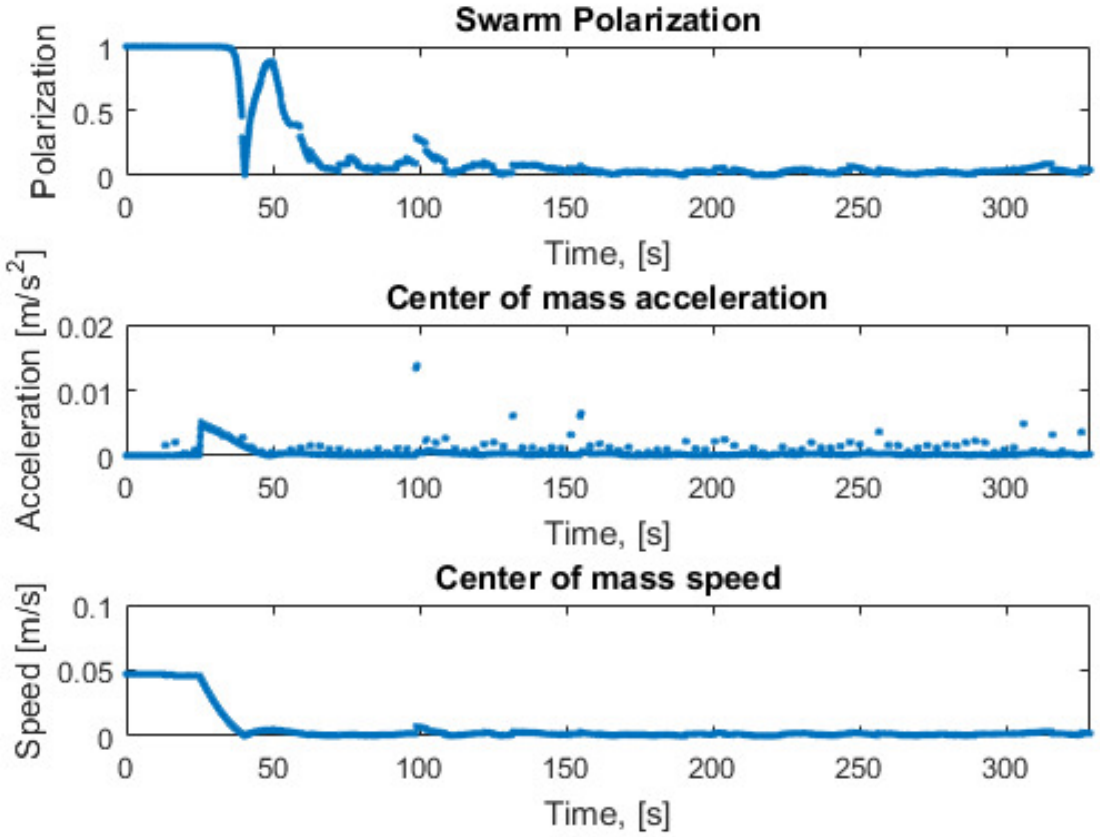

FIG. 15: Swarm polarization, center of mass acceleration, and center of mass speed for the ASV swarm using local sigmoidal repulsion[73] during a mixed reality experiment. A delay of 10s was introduced at t = 25s causing a translating to ring transition. The spike in polarization at t = 50s is caused by the agents momentarily reversing direction and translating in an aligned formation before breaking up.

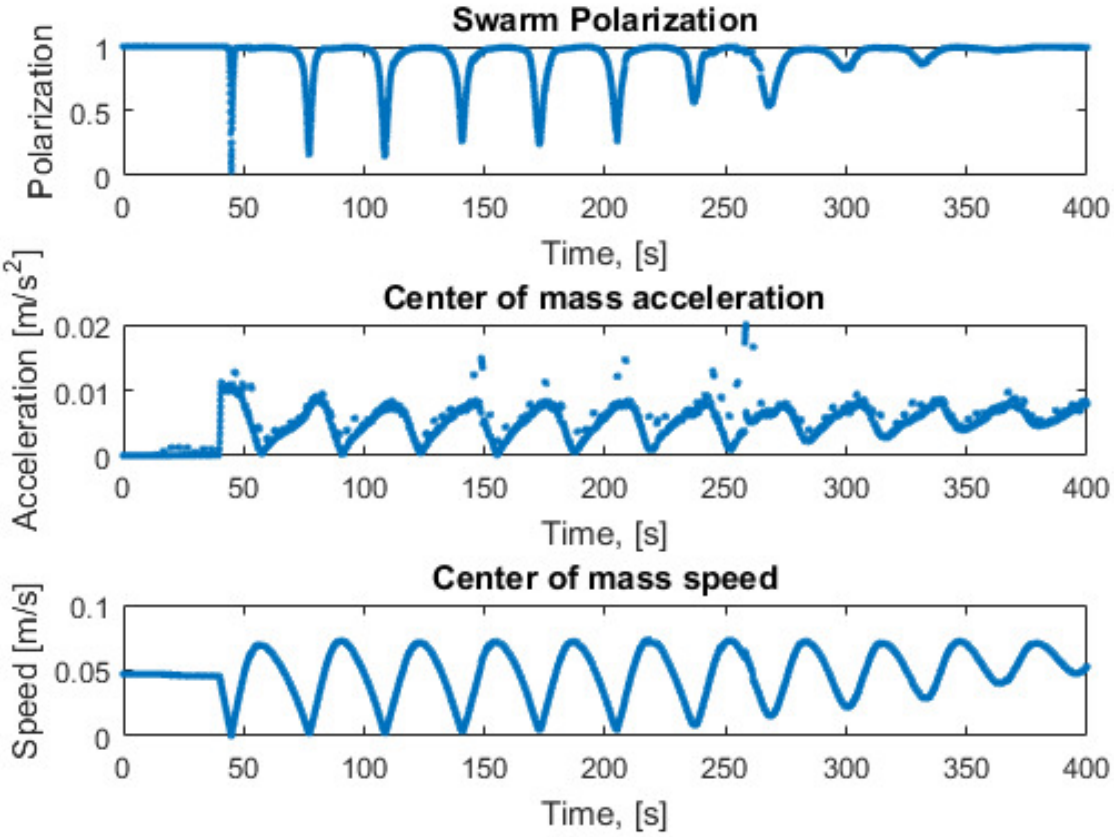

FIG. 16: Swarm polarization, center of mass acceleration, and center of mass speed for ASV swarm using sensed sigmoidal repulsion[73] during a mixed reality experiments. A delay of 35s was introduced at t = 40s causing a translating to rotating transition. The dips in swarm polarization were caused by the agents disagreeing on which way to turn in the early stages of the transition, where the agents were in a degenerate rotating state (one characterized by the swarm moving back and forth along a line). As the eccentricity of the ellipse lessened, more agents agreed on which direction to turn at the vertices of the ellipse.

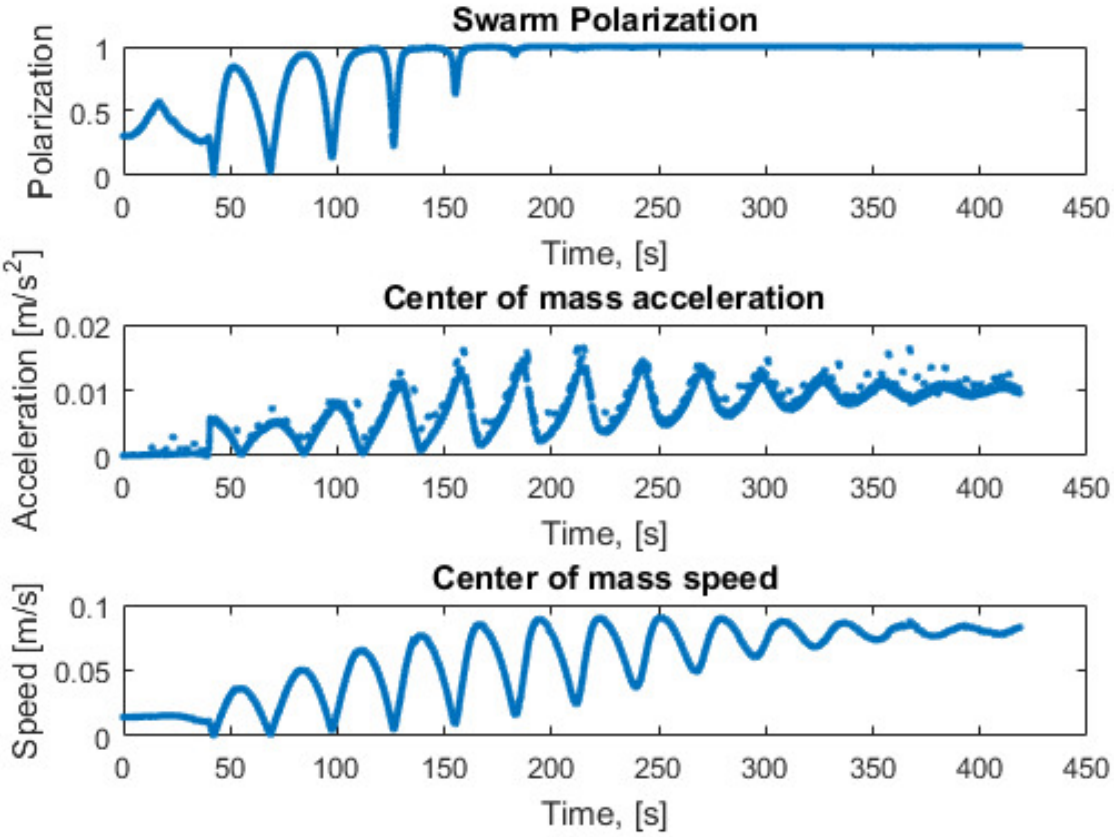

FIG. 17: Swarm polarization, center of mass acceleration, and center of mass speed for the ASV swarm using global sigmoidal repulsion[73] during a mixed reality experiment. A delay of 40s was introduced at t = 60s causing a ring to rotating swarm state transition. The oscillation in all measures was the result of the motion of the agents moving on a gradually widening ellipse. When the eccentricity of the ellipse was high, the agents slowed down as they changed direction (not necessarily the same direction) at the ends of the ellipse, and sped up near the center of the ellipse. This behavior gradually smoothed out as the motion approached that of a circle for large t.

III. COLLIDING SWARMS - USING ONE SWARM TO CONTROL ANOTHER

A. Introduction

Because of the robustness, scalability, and collective-problem solving capabilities of natural swarms, much research has focused on designing and building swarms of mobile robots with a large and ever expanding number of platforms, as well as virtual and physical interaction mechanisms[79,87–90]. Applications for such systems range from exploration[88], mapping[12], resource allocation[15,91,92], and swarms for defense[93–95]

Since the overall cost of robotic systems has decreased significantly in recent years, it has become possible to use artificial swarms in the real world[88,89,96,97]. This introduces the possibility of having multiple swarms occupying the same physical space, resulting in mutual interactions and perturbations of one another's dynamics[98]. As the potential for such swarm-on-swarm interactions increases, an understanding of how multiple swarms collide and merge becomes necessary.

Though much is known about the behaviors and stability of single isolated swarms with physically-inspired, nonlinear interactions[26,99–102], much less is known about the intersecting dynamics of multiple such swarms, even in the case where one swarm is a single particle, as in predator–prey modeling[103]. Recent numerical studies have shown that when two flocking swarms collide, the resulting dynamics typically appears as a merging of the swarms into a single flock, milling as one uniform swarm, or scattering into separate composite flocks moving in different directions[98,104,105]. Though interesting, a more detailed analytical understanding of how and when these behaviors occur is needed, especially when designing robotics experiments, and controlling their outcomes.

To make progress, we consider a generic system of mobile agents moving under the influence of self-propulsion, friction, and pairwise interaction forces. In the absence of interactions, each swarmer tends to a fixed speed, which balances its self-propulsion and friction but has no preferred direction[106]. A simple model that captures the basic physics is

$$\ddot{\mathbf{r}}_i = \left[\alpha_i - \beta|\dot{\mathbf{r}}_i|^2\right]\dot{\mathbf{r}}_i - \lambda_i \sum_{j\neq i} \partial_{\mathbf{r}_i} U(|\mathbf{r}_j - \mathbf{r}_i|) \tag{23}$$

where $\mathbf{r}_i$ is the position-vector for the ith agent in two spatial dimensions, α_i is a self-propulsion constant, β is a friction constant, and λ_i is a coupling constant[26,99–102]. Beyond providing a basis for theoretical insights, Eq.(23) has been implemented in experiments with several robotics platforms including autonomous cars, boats, and quad-rotors[107–109].

An example interaction potential that we consider in detail is the Morse potential,

$$U(r) = Ce^{-r/l} - e^{-r} \tag{24}$$

– a common model for soft-core interactions with local repulsion and attraction ranges, scaled as l and 1, respectively[102,110]. In the following, we assume that two interacting swarms are subject to the same underlying physics, Eqs.(23-24), but with different initial conditions and control parameters. In particular, we assume that within each swarm the parameters are homogeneous, e.g., $\alpha_i \in \{\alpha^{(1)}, \alpha^{(2)}\}$ and $\lambda_i \in \{\lambda^{(1)}, \lambda^{(2)}\}$, where the superscripts (1) and (2) denote the first and second swarm, respectively. Lastly, the total number of swarming agents is N.

B. Collision of two flocking swarms

As in[104,105], we are interested in the collision of two flocking swarms composed of approximately equal numbers of agents (in the absence of any communication delay). Initially the swarms are each prepared in a flocking state a large distance D from the collision region, such that $\mathbf{r}_i = \mathbf{d}_i^{(1)} - D\,\hat{\mathbf{x}}$ and $\dot{\mathbf{r}}_i = \sqrt{\alpha^{(1)}/\beta}\,\hat{\mathbf{x}}$ if $i \in (1)$, and $\mathbf{r}_i = \mathbf{d}_i^{(2)} + D\sqrt{\alpha^{(2)}/\alpha^{(1)}}(\cos(\theta)\hat{\mathbf{x}} + \sin(\theta)\hat{\mathbf{y}})$ and $\dot{\mathbf{r}}_i = \sqrt{\alpha^{(2)}/\beta}(-\cos(\theta)\hat{\mathbf{x}} + \sin(\theta)\hat{\mathbf{y}})$ if $i \in (2)$. The internal flocking coordinates, $\mathbf{d}_i^{(1)}$ and $\mathbf{d}_i^{(2)}$, represent local minimum energy configurations (MECs), $-\partial_{\mathbf{d}_i} U(|\mathbf{d}_j - \mathbf{d}_i|) = \mathbf{0}_i \ \forall i$. Before colliding, the swarms are assumed to be far apart, $D \gg 1$, with a collision angle θ. Note that given this setup, the net force on every agent is initially zero (a consequence of the MEC and the finite-range of interactions) and the swarms collide near the origin.

For relatively small θ the two flocks typically scatter or mill depending on the coupling strength. In the former the swarms leave the collision region in separate flocking states with perturbed velocities. In the latter they form a milling state, and circulate around a stationary center of mass. Figure 18(a) gives an example scattering diagram for the collision of symmetric flocks with equal parameters. The two final swarm states are specified with blue and red for scattering and milling, respectively; the green portions indicate the formation of a combined flocking state, which is comparatively infrequent. For small θ we can see that the combined milling state (MS) appears for couplings above a certain value λ_{min}. This *critical coupling* will be a primary focus in what follows.

In order to visualize collisions that result in milling states, we show four time-snapshots in Figure 18(b) when $\lambda = \lambda_{min}$. Agents in the two swarms are drawn with different colors, and their

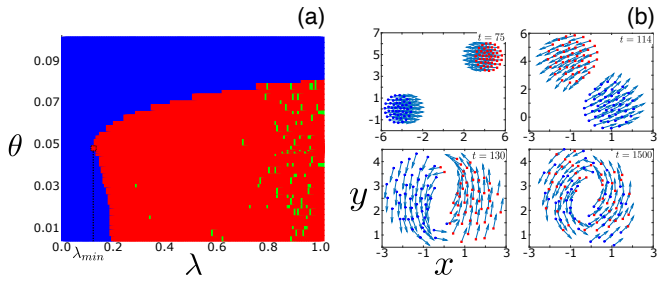

FIG. 18: Collision of two symmetric flocks. (a) Scattering digram indicating the final, aggregate swarm state as a function of the collision angle and coupling: scattering (blue), milling (red), and single-flock (green). The critical coupling is specified with a dashed vertical line, and separates the scattering and milling regions. (b) Four time-snapshots for $\lambda = \lambda_{min}$ showing each swarm with different colors: red squares and blue circles. Velocities are drawn with arrows. Swarm parameters are $\alpha = 1$, $\beta = 5$, $C = 10/9$, $l = 0.75$, and $N = 100$.

velocities shown with arrows. In the first snapshot (upper left), the swarms approach collision with configurations and velocities identical to those specified in the first paragraph of this section– namely, the MEC with constant velocity. In the second snapshot (upper right) the swarms rotate around each other with a constantly changing heading, roughly uniform velocity distribution, and a configuration approximately equal to the MEC. Over time each swarm's density elongates in the direction of rotation (third snapshot, lower left), as the velocity distribution becomes less homogeneous. Finally, on long times scales the two swarms blend into one and form a MS with agents from each uniformly distributed across the whole.

In order to predict the critical coupling, λ_{min}, our approach is to find an analytical description of the collision dynamics that is applicable for the first two snapshots in Figure 18(b), where two approximately MEC flocks approach, and then rotate around a common center. Our conjecture is that if such rotations are approximately stable, then a MS occurs upon collision (and visa versa). Though we will analyze two-flock collisions assuming Morse-potential interactions, Eq.(24), our method should be applicable to a broad range of second-order dynamical swarms given position-dependent, nonlinear interactions with finite attractive and repulsive length scales.

1. Uniform constant density approximation

First, we would like to find a low-dimensional approximation for the flocking state dynamics. A clue comes from Figure 19(a), which plots the fraction of nodes at a given distance r from the

center of mass (CM) of a single moving flock for different values of the repulsion strength, C. We can see that the radial distribution is approximately *linear* in r. Moreover, since the potential is radial, we expect the steady-state angular distribution to be uniform; the inlet panel shows an example flocking state with such a spatial distribution of agents. Together, these imply a roughly uniform density in the flocking state, $\rho = N/\pi R^2$, where R is the maximum radius. Given the uniform-density assumption, the predicted fraction of agents at a given r is $f(r) = 2r\Delta r/R^2$, where Δr is the bin-size used to plot the distribution. This prediction is drawn with lines in Figure 19(a).

Assuming a uniform density, we can describe a flock in general by its CM-dynamics and the boundary radius, R. In particular, every agent, including those on the boundary, move with constant speed, $\sqrt{\alpha/\beta}$, where α is the self-propulsion constant for the flock. A self-consistent formula can be derived for R, and used to compute it, by satisfying force-balance on the boundary. For instance, consider an agent with $\mathbf{d}_i = R\,\hat{\mathbf{x}}$. The x-component of the interaction force must be zero,

$$0 = \int_0^{2\pi}\int_0^1 \left(\frac{C}{l} e^{-\frac{R}{l}\sqrt{1+u^2-2u\cos\phi}} - e^{-\sqrt{1+u^2-2u\cos\phi}} \right) \cdot \frac{u\cos\phi - 1}{\sqrt{1+u^2-2u\cos\phi}} \cdot u\,du\,d\phi \;, \tag{25}$$

where $u \equiv r/R$. Note that the y-component of the force is trivially zero due to the uniform-angular distribution of agents. Comparisons between simulations and numerical solutions to Eq.(25) are shown in Fig.19(b) for a range of control parameters, and indicate good agreement.

Next, we can approximate the initial collision dynamics of two flocks by assuming that the uniform density configuration is maintained within each flock, with a boundary given by Eq.(25). Namely, the mean-field collision-model that we will analyze below is of two interacting, constant-density disks composed of self-propelled particles. Consider an agent positioned at the CM of each swarm, $\mathbf{r}^{(1)}(t)$ and $\mathbf{r}^{(2)}(t)$. Such agents feel self-propulsion, friction, and interaction forces, just as in Eq.(23). However, the non-zero contribution for the latter only comes from the *other flock*, since the interaction force from its own cancels out. Moreover, the force from the opposing flock is felt gradually as the two swarms approach, because of the finite range. To find the non-zero contribution, we simply need to integrate the interaction force over a constant-density disk of radius R, centered on the opposing swarm's CM. If we assume that the two swarms are roughly

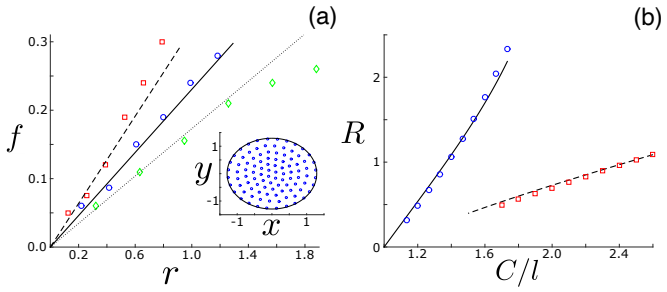

FIG. 19: Uniform constant density approximation for flocking states (UCDA). (a) fraction of agents a distance r from the flock's center of mass for $C=1.0$ (red-squares), 1.1 (blue-circles), 1.25 (green-diamonds) when $l=0.75$. The dashed, solid, and dotted lines indicate UCDA predictions. The inlet panel shows an example flocking state with the UCDA boundary drawn in black for $C=1.1$. (b) Flocking state boundary, $R=\max\{r\}$, from simulations ($l=0.75$, blue-circles) and ($l=0.50$, red-squares) compared to UCDA predictions (solid and dashed lines, respectively). Other swarm parameters are $\alpha=1$, $\beta=5$, $\lambda=2$, and $N=100$.

equally sized, each with $N/2$ agents, the CM-dynamics become

$$\ddot{\mathbf{r}}^{(1)} = \left[\alpha^{(1)} - \beta|\dot{\mathbf{r}}^{(1)}|^2\right]\dot{\mathbf{r}}^{(1)} - \frac{\lambda^{(1)}N}{2}\mathscr{E}(\mathbf{r}^{(2)},\mathbf{r}^{(1)};R) \tag{26a}$$

$$\ddot{\mathbf{r}}^{(2)} = \left[\alpha^{(2)} - \beta|\dot{\mathbf{r}}^{(2)}|^2\right]\dot{\mathbf{r}}^{(2)} - \frac{\lambda^{(2)}N}{2}\mathscr{E}(\mathbf{r}^{(1)},\mathbf{r}^{(2)};R) \tag{26b}$$

$$\mathscr{E}(\mathbf{r}^{(2)},\mathbf{r}^{(1)};R) = \int_0^{2\pi}\int_0^R \frac{\mathbf{r}^{(2)}+\mathbf{d}-\mathbf{r}^{(1)}}{|\mathbf{r}^{(2)}+\mathbf{d}-\mathbf{r}^{(1)}|}\cdot\frac{rdrd\phi}{\pi R^2} \cdot\left(\frac{C}{l}e^{-|\mathbf{r}^{(2)}+\mathbf{d}-\mathbf{r}^{(1)}|/l} - e^{-|\mathbf{r}^{(2)}+\mathbf{d}-\mathbf{r}^{(1)}|}\right) \tag{26c}$$

$$\mathbf{d} = r\cos\phi\ \hat{\mathbf{x}} + r\sin\phi\ \hat{\mathbf{y}}, \tag{26d}$$

where $\mathbf{d}$ is an internal-coordinate inside the constant-density disk centered on the opposing swarm's CM. Equations (25-26d) constitute the dynamical system that we call the uniform constant density approximation (UCDA). The integrals in Eq.(26c) can be evaluated using e.g., trapezoid rule with 100 discretization points. Our next step is to study stable oscillations in the UCDA and compare to swarm collision dynamics.

2. *Stable oscillations*

Stable oscillations in the UCDA come in the form of circular-orbit limit cycles where both flocks oscillate around a common center with the same frequency, a fixed phase difference, and different amplitudes in general. We can compute the parameters for such limit cycles by substituting the ansatz $\mathbf{r}^{(1)}(t) = R_1\cos(\omega t)\hat{\mathbf{x}} + R_1\sin(\omega t)\hat{\mathbf{y}}$ and $\mathbf{r}^{(2)}(t) = R_2\cos(\omega t+\gamma)\hat{\mathbf{x}} + R_2\sin(\omega t+\gamma)\hat{\mathbf{y}}$ into Eqs.(26a-26d). The result is the following four fixed-point equations:

$$0 = -R_1\omega^2 + \frac{\lambda^{(1)}N}{2}\mathscr{E}_x \tag{27a}$$

$$0 = -R_1\omega\left[\alpha^{(1)} - \beta R_1^2\omega^2\right] + \frac{\lambda^{(1)}N}{2}\mathscr{E}_y \tag{27b}$$

$$0 = -R_2\omega\sin\gamma\left[\alpha^{(2)} - \beta R_2^2\omega^2\right] + R_2\omega^2\cos\gamma + \frac{\lambda^{(2)}N}{2}\mathscr{E}_x \tag{27c}$$

$$0 = R_2\omega\cos\gamma\left[\alpha^{(2)} - \beta R_2^2\omega^2\right] + R_2\omega^2\sin\gamma + \frac{\lambda^{(2)}N}{2}\mathscr{E}_y \tag{27d}$$

with

$$\mathscr{E}_x = \int_0^{2\pi}\int_0^R \frac{R_2\cos\gamma + r\cos\phi - R_1}{d}\cdot\left(\frac{C}{l}e^{-d/l} - e^{-d}\right) \cdot\frac{r\,dr\,d\phi}{\pi R^2} \tag{27e}$$

$$\mathscr{E}_y = \int_0^{2\pi}\int_0^R \frac{R_2\sin\gamma + r\sin\phi}{d}\cdot\left(\frac{C}{l}e^{-d/l} - e^{-d}\right) \cdot\frac{r\,dr\,d\phi}{\pi R^2} \tag{27f}$$

$$d = \sqrt{(R_2\cos\gamma + r\cos\phi - R_1)^2 + (R_2\sin\gamma + r\sin\phi)^2}. \tag{27g}$$

Solutions to Eqs.(27a-27g) can be shown to exactly match limit cycles in the UCDA; more importantly, they agree with the transient oscillations for collisions in the full system, Eqs.(23-24). For example, Fig.20(a) shows CM-trajectories in red and blue for two colliding swarms when $\lambda = \lambda_{min}$. We can see that the trajectories approach the UCDA limit-cycle, shown with a black-dashed line, before slowly decaying into the origin. Using this picture as a basis, the maximum rotation radius during collisions can be compared directly to limit-cycle radii predictions from Eqs.(27a-27g). In Fig.20(b) we plot such a comparison using the maximum horizontal distance reached by the CM of the rightward moving flock (as a proxy for the collision radius). Mean-field predictions and simulations quantitatively agree fairly well over a broad range of parameter values. Qualitatively, as the repulsive-force constant C increases, the two swarms oscillate at

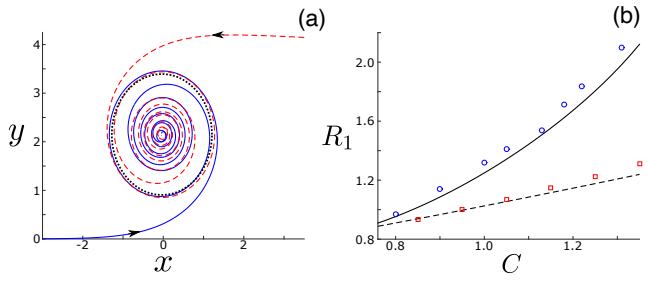

FIG. 20: Collision dynamics resulting in milling. (a) Center-of-mass trajectories for two colliding swarms when $\lambda = \lambda_{min}$, shown with solid-blue and dashed-red lines. Arrows give the direction of motion. The dashed-black line indicates the bifurcating limit cycle in the uniform constant density approximation. (b) Maximum x-coordinate reached by the center of mass of the rightward moving (blue) flock when $\lambda = \lambda_{min}$. Simulation results are shown with blue circles for $l = 0.75$ and red squares for $l = 0.5$. Limit-cycle predictions are drawn with solid and dashed lines, respectively. Other swarm parameters are $\alpha = 1$, $\beta = 5$, $l = 0.75$, and $N = 100$.

larger distances from each other upon collision, particularly for larger values of the repulsion scale, l. This increase in rotation distance, R_1, is accompanied by a decrease in rotation frequency, $\omega \sim R_1^{-1}$.

Next, we can consider stability. When control parameters are changed (one at a time), stable limit cycles satisfying Eqs.(27a-27g) disappear generically through *saddle-node bifurcations* (SNs). As stated previously in Sec.III B, a post-collision MS in the full system Eqs.(23-24) is not expected to form unless stable limit-cycles exist, and hence, λ_{min} can be approximated by the SN value in the UCDA. We can find a general condition to determine λ_{min} at the SN through the following. First, define a four dimensional vector consisting of the right-hand-side (RHS) of Eqs.(27a-27d), $\mathbf{F}$ = RHS([Eq.(27a),Eq.(27b),Eq.(27c),Eq.(27d)]). Second, compute the derivatives of $\mathbf{F}$ with respect to the limit-cycle parameters, $\mathbf{L} = [R_1, R_2, \gamma, \omega]$. Finally, at the SN the Jacobian matrix $\underline{J}$, defined as $J_{mn} \equiv \partial F_m / \partial L_n$, has $\det \underline{J} = 0$.

In practice, if we consider symmetric collisions or asymmetry in the α's only (as we do in the remainder), the above results simplify. For example, in the case of symmetric collisions the relevant branch of stable limit cycles have $R_1 = R_2$, $\gamma = \pi$, and $\omega = \sqrt{\alpha/\beta}/R_1$. Moreover, the

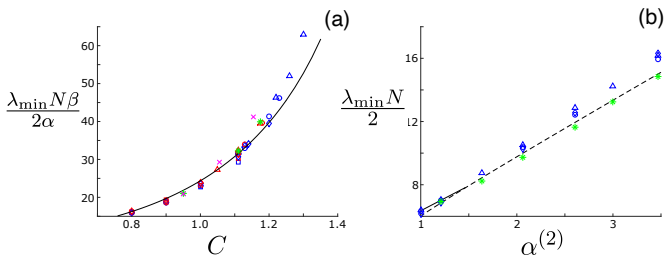

FIG. 21: Critical coupling for forming milling states upon collision. (a) Symmetric parameter collisions for $\alpha = 1$ (blue) and $\alpha = 2$ (red): $N = 10$ (squares), $N = 20$ (diamonds), $N = 40$ (circles), and $N = 100$ (triangles). Green stars denote $\alpha = 1$ and magenta x's denote $\alpha = 2$, when 40 agents collide with 60. (b) Asymmetric collisions for $C = 10/9$ in which $\alpha^{(1)} = 1$. Blue points indicate equal numbers in each flock: $N = 20$ (diamonds), $N = 40$ (circles), and $N = 100$ (triangles). Green stars denote collisions between 40 agents with $\alpha^{(1)} = 1$ and 60 agents with $\alpha^{(2)}$. Solid and dashed lines indicate theoretical predictions for (a) and (b), respectively. Other swarm parameters are $\beta = 5$ and $l = 0.75$.

critical coupling satisfies

$$\lambda_{min} = 2\alpha \Big/ N\beta R_1^2 \int_0^{2\pi}\int_0^R \frac{2rdrd\phi}{\pi R^2}\cdot\frac{\frac{C}{l}e^{-d/l}-e^{-d}}{d}\cdot \left[1-\frac{(2R_1-r\cos\phi)^2}{d^2}-\frac{(2R_1-r\cos\phi)^2}{d}\cdot\frac{\frac{C}{l^2}e^{-d/l}-e^{-d}}{\frac{C}{l}e^{-d/l}-e^{-d}}\right]. \tag{28}$$

An interesting consequence of the symmetric limit is the predicted scaling collapse, $\lambda_{min} N\beta/2\alpha = H(C,l)$, where the left hand side is a function of the pairwise-interaction parameters only. In addition, $\lambda_{min} \sim v^2$, where v is the speed of each flock, $\sqrt{\alpha/\beta}$.

Comparisons between the measured λ_{min} from scattering diagrams, e.g., Fig.18(a), and the above predictions are shown in Fig.21. In the left subplot (a), we show results for collisions with symmetric parameters with a large variety of N's and α's. As demonstrated with Eq.(28) our predicted scaling collapse, $\lambda_{min} N\beta/2\alpha = H(C,l)$, holds. Qualitatively, the critical coupling increases monotonically with C, implying that the stronger the strength of repulsion, the larger the coupling needs to be in order for colliding swarms to form a MS. Also, note that our mean-field predictions are fairly robust to heterogeneities in the numbers in each flock, particularly for smaller values of $C/l - 1$; predictions remain accurate for number heterogeneity as large as 20%.

On the other hand, in Fig.21(b) we compare the measured λ_{min} and predictions as a function of asymmetry in the self-propulsion force constant for different N's. The first swarm has $\alpha^{(1)} = 1$,

while $\alpha^{(2)}$ is varied. Contrary to the symmetric case the scaling collapse disappears, apart from N. Moreover, the branch of stable limit cycles with $R_1 = R_2$ disappears in a cusp bifurcation; the solid-black line vanishes for $\alpha^{(2)} \gtrsim 1.5$. The upper branch of SNs (shown with a dashed-black line) corresponds to stable limit cycles where $R_1 < R_2$ and $\gamma = -\pi/2$. Interestingly, we can see that for larger values of $\alpha^{(2)} - \alpha^{(1)}$ the critical coupling is nearly linear in the difference, meaning that if one flock doubles its speed, then the coupling needed to form an MS is expected to quadruple – again, a consequence of the flock speed equalling $\sqrt{\alpha/\beta}$. Finally, note that as in (a), predictions remain accurate for a significant range of differences in the numbers in each flock.

IV. CONCLUSIONS

We considered three basic open problems in autonomous swarm: How the stability of swarms changes as functions of system parameters in the presence of range dependent communication networks. The dynamics of current mixed-reality experiments of swarm patterns to verify previous bifurcation analysis. Finally, we showed how one swarm can change the behavior of another by colliding the two swarms.

Specifically, we considered a new model of a swarm with delay-coupled communication network, where the delay is considered to be range dependent. That is, given a range radius, delay is on if two agents are outside the radius and zero otherwise. The implication is that small delays do not matter if the agents are close to each other. The additional range dependence creates a new set of bifurcations not previously seen. For general swarms without delay, the usual states consist of flocking (translation) or ring/rotational state (milling), with agents spread in phase. With the addition of a fixed delay, a rotational state bifurcates that has all agents in phase and rotate together. Range dependence introduces a new rotational bifurcating state that exhibits behavior observed as a new mixed state combining dynamics of both ring and rotating states. The radius parameter, was used to quantify the bifurcation of the rotational mixed state. For small radii, we see that the dynamics for the full swarm shows clustered counter-rotational behavior that is periodic. This agrees for small radius values in the mean field description as well. As the radius increases, the mixed periodic state generates new frequencies in the full model, which are manifested as torus bifurcations in the mean field. Mean field analysis was done by tracking Floquet multipliers that cross the imaginary axis as complex pairs. Frequency analysis explicitly shows the additional frequencies in the mean field.

Finally, we tracked the locus of coupling amplitudes and delay for various values of radii locating the parameters at which torus bifurcation occur. The results reveal that as delay radius increases, torus bifurcations onset at lower values of coupling amplitude and delay. The implications are that more complicated behavior than periodic motion has a greater probability of being observed in both theory and experiment if range dependence of delay is included.

Through manipulating communication delay and coupling strength, we took the first significant steps to test different emergent swarm states using mixed reality. The mixed reality framework allowed for the study of emergent swarm behavior through the use of simulation to increase the number of agents while maintaining critical real world interactions, which are hard to model, with

physical platforms. Because mixed reality can handle many different levels of abstraction, we were able to use two distinct robotic platforms to validate the swarm behavior. We selected the level of abstraction necessary for the behavior to exhibit, and in our case, it was focused on agents that exhibited simple dynamics and used delayed information as would be done in the real world. Both the ASVs and the UAV tested all three of the theoretically predicted behaviors along with transitions between the predicted swarm states. This emphasizes that the proposed swarm model has the potential to be applicable across platforms and highlights the impacts of communication delay on systems behavior.

There is a range of theory that supports the proposed model, and the presented results are significant steps toward showing theory is valid as well as also demonstrating that there are areas of interest that the theory is not capturing. Understanding the multi-stability in this system is difficult analytically, but with the use of simulation and mixed reality, we were able to observe multi-stability and the impacts it has on the proposed theoretical model when paired with real vehicles.

The next steps for this work include investigating how the addition of more real world assumptions change the predicted emergent patterns. For example, our communication model of global coupling is not practical with all real robots due to network limitations. The next step is to study the impacts of range based communication. While often swarms are studied for homogeneous agents, it is also possible to consider the impacts of heterogeneity and this may require different types of collision avoidance to be used to account for different hardware limitations. Finally, there exist different dynamic models, where delay can be added. This presents new potential patterns to be studied using the described forms of analysis. These changes will continue to add to the understanding of our current models and the use of this type of emergent behavior in the physical world.

Finally, we studied the collision of two swarms with nonlinear interactions, and focused in particular on predicting when such swarms would combine to form a mill. Unlike the full scattering diagram, which depends on whether or not a particular set of initial conditions falls within the high-dimensional basin-of-attraction for milling (a hard problem in general), we concentrated on predicting the minimum coupling needed to sustain a mill for near head-on collisions. By noticing that collid- ing swarms, which eventually form a mill, initially rotate around a common center with an approximately constant density, we were able to transform the question of a crit- ical coupling into determining the stability of limit-cycle states within a mean-field approximation. Our

bifurca- tion analysis agreed with many-agent simulations. Though our analysis dealt directly with soft-core in- teracting swarms, the basic approach could be easily extended to a broader range of models, as long as the non- linear forces between agents have a finite range. Moreover, a straightforward way to improve the accuracy of our analysis would be to move beyond the uniform- density assumption, and replace it with an exact steady- state density for flocking states with general interactions. Beyond that, the next step for improvement would be to include the density dynamics directly, which may provide further insights for controlling swarm collisions, includ- ing in other setups such as flocks-vs-mills. Nevertheless, this work takes an important step toward understanding and analyzing nonlinear swarm collisions.

V. ACKOWLEDGEMENTS

JH, IBS were supported by and the Naval Innovative Science and Engineering award NISE OP-001214, the U.S. Naval Research Laboratory basic research funding (N0001419WX00055), the Office of Naval Research (N0001419WX01166) and (N0001419WX01322). TE was supported through the U.S Naval Research Laboratory Karles Fellowship and the NISE award.

REFERENCES

[1]E. O. Budrene and H. C. Berg, Nature **376**, 49 (1995).

[2]A. A. Polezhaev, R. A. Pashkov, A. I. Lobanov, and I. B. Petrov, The International Journal of Developmental Biology **50**, 309 (2006).

[3]R. M. Lee, D. H. Kelley, K. N. Nordstrom, N. T. Ouellette, and W. Losert, New Journal of Physics **15** (2013), 10.1088/1367-2630/15/2/025036.

[4]K. r. Tunstrø m, Y. Katz, C. C. Ioannou, C. Huepe, M. J. Lutz, and I. D. Couzin, PLoS computational biology **9**, e1002915 (2013).

[5]D. Helbing and P. Molnar, Physical Review E **51**, 4282 (1995).

[6]L. Giuggioli, T. J. McKetterick, and M. Holderied, PLOS Computational Biology **11**, e1004089 (2015).

[7]S.-H. Lee, Physics Letters A **357**, 270 (2006).

[8]C. M. Topaz and A. L. Bertozzi, SIAM Journal on Applied Mathematics **65**, 152 (2004).

[9]K. Szwaykowska, L. M.-y.-T. Romero, and I. B. Schwartz, IEEE Transactions on Automation Science and Engineering **12**, 810 (2015), arXiv:1409.1042.

[10]L. Mier-y-Teran Romero, E. Forgoston, and I. B. Schwartz, in *Proceedings of the IEEE/RSJ International Conference on Intelligent Robots and Systems* (2011) pp. 3905–3910.

[11]J. Hindes, K. Szwaykowska, and I. B. Schwartz, Phys. Rev. E **94**, 032306 (2016).

[12]R. K. Ramachandran, K. Elamvazhuthi, and S. Berman, "An optimal control approach to mapping gps-denied environments using a stochastic robotic swarm," in *Robotics Research: Volume 1*, edited by A. Bicchi and W. Burgard (Springer International Publishing, Cham, 2018) pp. 477–493.

[13]D. S. Morgan and I. B. Schwartz, Physics Letters A **340**, 121 (2005).

[14]J. Wiech, V. A. Eremeyev, and I. Giorgio, Continuum Mechanics and Thermodynamics **30**, 1091 (2018).

[15]H. Li, C. Feng, H. Ehrhard, Y. Shen, B. Cobos, F. Zhang, K. Elamvazhuthi, S. Berman, M. Haberland, and A. L. Bertozzi, in *2017 IEEE/RSJ International Conference on Intelligent Robots and Systems (IROS)* (2017) pp. 4341–4347.

[16]H. G. Tanner, A. Jadbabaie, and G. J. Pappas, IEEE Transactions on Automatic Control **52**, 863 (2007).

[17]V. Gazi, IEEE Transactions on Robotics **21**, 1208 (2005).

[18]A. Jadbabaie, Jie Lin, and A. S. Morse, IEEE Transactions on Automatic Control **48**, 988 (2003).

[19]C. Viragh, G. Vasarhelyi, N. Tarcai, Szorenyi, and et al, Bioinspiration & biomimetics **9**, 025012 (2014).

[20]J. P. Desai, J. P. Ostrowski, and V. Kumar, in *IEEE Transactions on Robotics and Automation*, Vol. 17(6) (2001) pp. 905–908.

[21]T. Vicsek, A. Czirok, E. Ben-Jacob, I. Cohen, and O. Shochet, "Novel type of phase transition in a system of self-driven particles," (2006), arXiv:0611743v1 [arXiv:cond-mat].

[22]L. Edelstein-Keshet, D. Grunbaum, and J. Watmough, Journal of Mathematical Biology **36**, 515 (1998).

[23]L. Giuggioli, T. McKetterick, and M. Holderied, PLoS Comput Biol **11** (2015).

[24]N. Nagy, Z. Akos, D. Biro, and T. Vicsek, Nature **464**, 890 (2010).

[25]J. Fehrenbach, J. Narski, J. Hua, S. Lemercier, A. Jelic, C. Appert-Rolland, S. Donikian, J. PettrÃl', and P. Degond, (2014), 10.3934/nhm.2015.10.579, arXiv:1412.7537.

[26]L. Mier-y-Teran Romero, E. Forgoston, and I. B. Schwartz, IEEE Transactions on Robotics **28**, 1034 (2012), arXiv:arXiv:1205.0195v1.

[27]K. Szwaykowska, I. B. Schwartz, L. Mier-y Teran Romero, C. R. Heckman, D. Mox, and M. A. Hsieh, Phys. Rev. E **93**, 032307 (2016).

[28]V. Edwards, P. deZonia, M. A. Hsieh, J. Hindes, I. Triandaf, and I. B. Schwartz (2020).

[29]J. Hindes and I. B. Schwartz, Chaos: An Interdisciplinary Journal of Nonlinear Science **28**, 071106 (2018), https://doi.org/10.1063/1.5041377.

[30]K. Szwaykowska, I. B. Schwartz, and T. W. Carr, in *11th International Symposium on Mechatronics and its Applications (ISMA)* (2018) pp. 1–6.

[31]M. Komareji, Y. Shang, and R. Bouffanais, Nonlinear Dynamics **93**, 1287 (2018).

[32]L. Oliveira, L. Almeida, and P. Lima, in *2015 IEEE World Conference on Factory Communication Systems (WFCS)* (2015) pp. 1–8.

[33]M. ying Ani Hsieh, P. Srivastava, V. Kumar, and C. J. Taylor, in *Mobile Robots XVII*, Vol. 5609, edited by D. W. Gage, International Society for Optics and Photonics (SPIE, 2004) pp. 192 – 200.

[34]M. A. Hsieh, A. Cowley, J. F. Keller, L. Chaimowicz, B. Grocholsky, V. Kumar, C. J. Taylor, Y. Endo, R. C. Arkin, B. Jung, D. F. Wolf, G. S. Sukhatme, and D. C. MacKenzie, Journal of Field Robotics **24**, 991 (2007), https://onlinelibrary.wiley.com/doi/pdf/10.1002/rob.20222.

[35]J. Fink, A. Ribeiro, and V. Kumar, Proceedings of the IEEE **100**, 164 (2012).

[36]J. Fink, A. Ribeiro, and V. Kumar, IEEE Access **1**, 290 (2013).

[37]F. Arrichiello, D. Liu, S. Yerramall, A. Pereira, J. Das, U. Mitra, and G. Sukhatme (2009).

[38]J. K. Hale, *Theory of Functional Differential Equations*, Applied Mathematical Sciences (Springer-Verlag, New York, 1977).

[39]F. Hartung, T. Krisztin, H. Walther, and J. Wu, "Chapter 5 functional differential equations with state-dependent delays: Theory and applications," in *Handbook of Differential Equations: Ordinary Differential Equations*, Handbook of Differential Equations: Ordinary Differential Equations, Vol. 3 (2006) pp. 435–545.

[40]J. K. Hale and S. M. V. Lunel, *Introduction to Functional Differential Equations* (Springer, New York, 1993).

[41]K. TunstrÃÿm, Y. Katz, C. C. Ioannou, C. Huepe, M. J. Lutz, and I. D. Couzin, PLOS Computational Biology **9**, 1 (2013).

[42]D. S. Calovi, U. Lopez, S. Ngo, C. Sire, H. Chaté, and G. Theraulaz, New Journal of Physics **16** (2014), 10.1088/1367-2630/16/1/015026, arXiv:1308.2889.

[43]N. E. Leonard, in *Handbook of Ocean Engineering, Part B: Autonomous Ocean Vehicles, Systems and Control*, edited by T. B. Curtin (Springer, New York, New York, USA, 2013) Chap. 9.

[44]A. Cavagna, L. Del Castello, I. Giardina, T. Grigera, A. Jelic, S. Melillo, T. Mora, L. Parisi, E. Silvestri, M. Viale, and A. M. Walczak, Journal of Statistical Physics **158**, 601 (2015).

[45]H. Ling, M. G. E., van der Vaart K., V. R. T., T. A., and O. N. T., "Local interactions and their group-level consequences in flocking jackdaws," (2019).

[46]J. Li and A. H. Sayed, EURASIP Journal on Advances in Signal Processing **2012**, 18 (2012).

[47]G. Theraulaz, E. Bonabeau, S. C. Nicolis, R. V. Solé, V. Fourcassié, S. Blanco, R. Fournier, J.-L. Joly, P. Fernández, A. Grimal, P. Dalle, and J.-L. Deneubourg, Proceedings of the National Academy of Sciences **99**, 9645 (2002), https://www.pnas.org/content/99/15/9645.full.pdf.

[48]C. M. Topaz, M. R. D'Orsogna, L. Edelstein-Keshet, and A. J. Bernoff, PLOS Computational Biology **8**, 1 (2012).

[49]K. Rio and W. H. Warren, Transportation Research Procedia **2**, 132 (2014), the Conference on Pedestrian and Evacuation Dynamics 2014 (PED 2014), 22-24 October 2014, Delft, The Netherlands.

[50]L. Jiang, L. Giuggioli, A. Perna, and et. al., PLoS Comput Biol **13**, e1005822 (2017).

[51]J. Hindes, V. Edwards, S. Kamimoto, I. Triandaf, and I. B. Schwartz, "Unstable oscillations and bistability in delay-coupled swarms," (2020), arXiv:2002.12420 [nlin.AO].

[52]I. B. Schwartz, V. Edwards, S. Kamimoto, K. Kasraie, I. Triandaf, M. A. Hsieh, and J. Hindes, "Torus bifurcations of large-scale swarms having range dependent communication delay," (2020), arXiv:2003.03591 [nlin.AO].

[53]H. G. Tanner, A. Jadbabaie, and G. J. Pappas, in *42nd IEEE International Conference on Decision and Control (IEEE Cat. No.03CH37475)*, Vol. 2 (2003) pp. 2010–2015 Vol.2.

[54]H. G. Tanner, A. Jadbabaie, and G. J. Pappas, in *42nd IEEE International Conference on Decision and Control (IEEE Cat. No.03CH37475)*, Vol. 2 (2003) pp. 2016–2021 Vol.2.

[55]C. Viragh, G. Vasarhelyi, N. Tarcai, T. Szorenyi, G. Somorjai, T. Nepusz, and T. Vicsec, Bioinspir Biomim (2014).

[56]L. M. y Teran-Romero and I. B. Schwartz, EPL (Europhysics Letters) **105**, 20002 (2014).

[57]M. I. Freidlin and A. D. Wentzell, "Random perturbations," in *Random Perturbations of Dynamical Systems* (Springer New York, New York, NY, 1998) pp. 15–43.

[58]D. K. Wells, W. L. Kath, and A. E. Motter, Phys. Rev. X **5**, 031036 (2015).

[59]H. Hartle and R. Wackerbauer, Phys. Rev. E **96**, 032223 (2017).

[60]G. Ansmann, K. Lehnertz, and U. Feudel, Phys. Rev. X **6**, 011030 (2016).

[61]M. Rubenstein, C. Ahler, and R. Nagpal, in *2012 IEEE International Conference on Robotics and Automation* (2012) pp. 3293–3298.

[62]J. A. Preiss, W. Honig, G. S. Sukhatme, and N. Ayanian, in *2017 IEEE International Conference on Robotics and Automation (ICRA)* (2017) pp. 3299–3304.

[63]D. Pickem, P. Glotfelter, L. Wang, M. Mote, A. Ames, E. Feron, and M. Egerstedt, in *2017 IEEE International Conference on Robotics and Automation (ICRA)* (2017) pp. 1699–1706.

[64]M. Dorigo, D. Floreano, L. M. Gambardella, F. Mondada, S. Nolfi, T. Baaboura, M. Birattari, M. Bonani, M. Brambilla, A. Brutschy, D. Burnier, A. Campo, A. L. Christensen, A. Decugniere, G. Di Caro, F. Ducatelle, E. Ferrante, A. Forster, J. M. Gonzales, J. Guzzi, V. Longchamp, S. Magnenat, N. Mathews, M. Montes de Oca, R. O'Grady, C. Pinciroli, G. Pini, P. Retornaz, J. Roberts, V. Sperati, T. Stirling, A. Stranieri, T. Stutzle, V. Trianni, E. Tuci, A. E. Turgut, and F. Vaussard, IEEE Robotics & Automation Magazine **20**, 60 (2013).

[65]D. Ipparthi, A. Winslow, M. Sitti, M. Dorigo, and M. Mastrangeli, Soft Matter **13**, 7595 (2017).

[66]R. Warkentin, W. Savoie, and D. Goldman, (2018).

[67]W. Honig, C. Milanes, L. Scaria, T. Phan, M. Bolas, and N. Ayanian, in *2015 IEEE/RSJ International Conference on Intelligent Robots and Systems (IROS)* (2015) pp. 5382–5387.

[68]V. Edwards, P. Gaskell, and E. Olson, in *Proceedings of the 17th International Conference on Autonomous Agents and MultiAgent Systems*, AAMAS '18 (International Foundation for Autonomous Agents and Multiagent Systems, Richland, SC, 2018) pp. 2183–2185.

[69]M. Quinlan, T.-C. Au, J. Zhu, N. Stiurca, and P. Stone, in *2010 IEEE/RSJ International Conference on Intelligent Robots and Systems* (2010) pp. 6083–6088.

[70]B. Huang, B. Deniz, N. Gopalan, and S. Tellex, in *International Conference on Robotics and Automation*, ICRA 2019 (2019).

[71]E. Rosen, D. Whitney, E. Phillips, G. Chien, J. Tompkin, G. Konidaris, and S. Tellex, The International Journal of Robotics Research **0**, 0278364919842925 (0), https://doi.org/10.1177/0278364919842925.

[72]D. Mellinger and V. Kumar, in *2011 IEEE International Conference on Robotics and Automation* (2011) pp. 2520–2525.

[73]Three different variants of sigmoid repulsion were tested, where current robot position data was used in each case. The first type was global sigmoid repulsion, where all agents had delayed attraction and an infinite range of repulsion. The next type was local sigmoid repulsion, where all agents had delayed attraction and a finite range of repulsion. Finally there was sensed sigmoid repulsion, where all agents had delayed attraction outside a simulated local sensing radius and up-to-date information within that radius with finite range repulsion. Sensed sigmoid repulsion attempts to emulate a realistic interaction model where agents make full use of their sensors by fusing communicated and sensed position data about other agents. Four experiments were run using each type of repulsion: global, local, and sensed sigmoid repulsion. The collision avoidance parameters used were $c_r = 0.0067\,\mathrm{m/s^2}$, $R_{rep} = 0.1\,\mathrm{m}$, and $k = 40$.

[74]D. Armbruster, S. Martin, and A. Thatcher, Physica D: Nonlinear Phenomena **344** (2016), 10.1016/j.physd.2016.11.008.

[75]K. Tunstrøm, Y. Katz, C. C. Ioannou, C. Huepe, M. J. Lutz, and I. D. Couzin, in *PLoS Computational Biology* (2013).

[76]A. Polezhaev, R. Pashkov, A. I. Lobanov, and I. B. Petrov, Int. J. Dev. Bio. **50**, 309 (2006).

[77]C. M. Topaz, M. R. D'Orsogna, L. Edelstein-Keshet, and A. J. Bernoff, PLoS Comput. Biol. **8**, 1 (2012).

[78]M. Ballerini, N. Cabibbo, R. Candelier, A. Cavagna, E. Cisbani, I. Giardina, V. Lecomte, A. Orlandi, G. Parisi, A. Procaccini, M. Viale, and V. Zdravkovic, Proceedings of the National Academy of Sciences **105**, 1232 (2008), https://www.pnas.org/content/105/4/1232.full.pdf.

[79]F. Cichos, K. Gustavsson, B. Mehlig, and G. Volpe, Nature Machine Intelligence **2**, 94 (2020).

[80]T. Vicsek and A. Zafeiris, Phys. Rep. **517**, 71 (2012).

[81]M. C. Marchetti, J. F. Joanny, S. Ramaswamy, T. B. Liverpool, J. Prost, M. Rao, and R. A. Simha, Rev. Mod. Phys. **85**, 1143 (2013).

[82]M. Aldana, V. Dossetti, C. Huepe, V. M. Kenkre, and H. Larralde, Phys. Rev. Letts. **98**, 095702 (2007).

[83]A. Solon, Y. Fily, A. Baskaran, M. E. Cates, Y. Kafri, M. Kardar, and J. Tailleur, Nature Phys. **11**, 673 (2015).

[84]E. Fodor, C. Nardini, M. E. Cates, J. Tailleur, P. Visco, and F. van Wijland, Phys. Rev. Lett. **117**, 038103 (2016).

[85]F. G. Woodhouse, H. Ronellenfitsch, and J. Dunkel, Phys. Rev. Lett. **121**, 178001 (2018).

[86]E. Woillez, Y. Zhao, Y. Kafri, V. Lecomte, and J. Tailleur, Phys. Rev. Lett. **122**, 258001 (2019).

[87]R. Siegwart, I. Nourbakhsh, and D. Scaramuzza, *Autonomous Mobile Robots* (MIT Press, London, 2011).

[88]I. D. Miller, F. Cladera, A. Cowley, S. S. Shivakumar, E. S. Lee, L. Jarin-Lipschitz, A. Bhat, N. Rodrigues, A. Zhou, A. Cohen, A. Kulkarni, J. Laney, C. J. Taylor, and V. Kumar, IEEE Robotics and Automation Letters **5**, 2840 (2020).

[89]D. Pickem, P. Glotfelter, L. Wang, M. Mote, A. Ames, E. Feron, and M. Egerstedt, in *2017 IEEE International Conference on Robotics and Automation (ICRA)* (2017) pp. 1699–1706.

[90]E. Kagan, N. Shvalb, and I. Ben-Gal, *Autonomous Mobile Robots and Multi-Robot Systems: Motion-Planning, Communication, and Swarming* (Wiley, Hoboken, NJ, 2020).

[91]S. Berman, A. Halasz, V. Kumar, and S. Pratt, in *Proceedings 2007 IEEE International Conference on Robotics and Automation* (2007) pp. 2318–2323.

[92]M. A. Hsieh, V. Kumar, and L. Chaimowicz, Robotica **26**, 1 (2008).

[93]W. K. Wong, S. Ye, H. Liu, and Y. Wang, Mobile Networks and Applications (2020), 10.1007/s11036-020-01628-x.

[94]H. Chung, S. Oh, D. H. Shim, and S. S. Sastry, Proceedings of the IEEE **99**, 1562 (2011).

[95]U. Witkowski and M. E. Habbal, 6th Framework program of European Union.

[96]M. Rubenstein, C. Ahler, and R. Nagpal, in *2012 IEEE International Conference on Robotics and Automation* (2012) pp. 3293–3298.

[97]K. Petersen, R. Nagpal, and J. Werfel, in *Conference: Robotics: Science and Systems VII* (2012) pp. 3293–3298.

[98]G. Sartoretti and M.-O. Hongler, Entropy **18** (2016), 10.3390/e18010027.

[99]H. Levine, W. J. Rappel, and I. Cohen, Phys. Rev. E **63**, 017101 (2000).

[100]U. Erdmann, W. Ebeling, and A. S. Mikhailov, Phys. Rev. E **71**, 051904 (2005).

[101]E. Minguzzi, European Journal of Physics **36**, 035014 (2015).

[102]M. R. D'Orsogna, Y. L. Chuang, A. L. Bertozzi, and L. S. Chayes, Phys. Rev. Lett. **96**, 104302 (2006).

[103]Y. Chen and T. Kolokolnikov, Journal of the Royal Society, Interface **11**, 20131208 (2014).

[104]D. Armbruster, S. Martin, and A. Thatcher, Physica D: Nonlinear Phenomena **344**, 45 (2017).

[105]C. Kolon and I. B. Schwartz, arXiv preprint arXiv:1803.08817 (2018).

[106]J. Hindes, V. Edwards, S. Kamimoto, G. Stantchev, and I. B. Schwartz, Physical Review E **102**, 022212 (2020).

[107]K. Szwaykowska, I. B. Schwartz, L. M.-y.-T. Romero, C. R. Heckman, D. Mox, and M. A. Hsieh, Physical Review E **93**, 032307 (2016).

[108]V. Edwards, P. deZonia, M. A. Hsieh, J. Hindes, I. Triandaf, and I. B. Schwartz, Chaos **30**, 073126 (2020).

[109]J. Hindes, V. Edwards, S. Kamimoto, I. Triandaf, and I. B. Schwartz, "Unstable oscillations and bistability in delay-coupled swarms," (2020), arXiv:2002.12420 [nlin.AO].

[110]A. Bernoff and C. Topaz, SIAM Journal of Applied Dynamical Systems **10**, 212 (2011).